

# Report

---

## Electrochemical Processes of the High-Temperature-CO<sub>2</sub>-Electrolysis

---

Institute of Energy and Climate Research (IEK9)  
At the Forschungszentrum Jülich

Submitted by  
Fatma Ülkü Öztas  
Student ID: 369950  
Jülich, September 2020

Supervision  
Prof. Dr. Rüdiger Eichel  
Lucy Dittrich

## Content

1	Introduction .....	1
2	Theoretical Background .....	3
2.1	High-Temperature Electrolysis of CO <sub>2</sub> using SOECs .....	3
2.2	Electrochemical Basics .....	5
2.2.1	Open Cell Voltage .....	5
	where E <sup>0</sup> is the standard cell voltage, F the Faraday's constant, R the ideal gas constant (8.3145 J mol <sup>-1</sup> K <sup>-1</sup> ), T the operating temperature and p the partial pressure of the specific gases at the electrode surface. <sup>[11]</sup> .....	5
2.2.2	Polarization Processes .....	5
2.3	Electrochemical Characterization .....	6
2.3.1	i/V Characterization .....	6
2.3.2	Electrochemical Impedance Spectroscopy (EIS) .....	7
2.3.2.1	Fundamentals .....	7
2.3.2.2	Data Presentation.....	8
2.3.2.3	Kramers-Kronig Test.....	9
2.3.2.4	Elementary Analysis .....	9
2.3.2.5	Distribution of Relaxation Times .....	10
3	State of the Art .....	12
4	Experimental .....	14
4.1	Setup.....	14
4.2	Full-Cell .....	14
4.3	Reduction of NiO .....	14
4.4	Electrochemical Measurements.....	15
5	Results and Discussion.....	17
5.1	i/V Curves .....	17
5.2	Impedance Spectroscopy .....	20
5.2.1	Temperature Dependence.....	21
5.2.2	Current Density Dependence .....	29

5.2.3	50 % CO <sub>2</sub> and 50 % CO .....	33
6	Conclusion and Outlook.....	37
7	References .....	39
8	Appendix .....	41

# 1 Introduction

One of the main challenges today is the climate change. Although our planet's climate has constantly been changing throughout earth's history, the current period of warming is occurring more rapidly than many past events. In 2015, the governments of more than 190 nations gathered to find a solution to slow down this process. This conference resulted in the Paris Agreement, in which they committed on the reduction of anthropogenic greenhouse gases, such as CO<sub>2</sub>.<sup>[1]</sup> Another big challenge is the imminent depletion of fossil fuels such as coal, oil and natural gas. It is problematic, since fossil fuels are used as both raw material and energy source.<sup>[2]</sup> Although renewable alternative energy resources have gained great interest in recent years, they are associated with a fundamental problem regarding the match of energy supply and demand. At this point, an efficient energy storage became essential.<sup>[3]</sup>

An attractive approach, which meets the mentioned challenges is the valorization of CO<sub>2</sub> by electrolysis. Utilization of the temporarily unused energy, generated by renewable sources, for the production of valuable chemicals is an effective storage system.<sup>[4]</sup>

Among various electrochemical approaches, solid oxide cells (SOC) are advanced electrochemical conversion and energy storage devices with high efficiencies. They can produce electricity in the fuel cell mode (SOFC) by oxidizing the feed and they can also utilize electricity to reduce the feed in the electrolysis mode (SOEC).<sup>[5]</sup> SOECs can operate in the temperature range from 500 to 900 °C, which is also referred to as high temperature (HT) electrolysis.

In recent years, an increasing focus on hydrogen as alternative energy carrier has attracted great attention for the HT electrolysis of steam. However, the current infrastructure is based upon liquid hydrocarbons rather than hydrogen.<sup>[6]</sup> In that regard, the simultaneous HT electrolysis of steam and carbon dioxide, which is known as co-electrolysis, is a promising method for the valorization of carbon dioxide and is at the same time independent of fossil fuels.

Besides pure steam and co-electrolysis, carbon dioxide electrolysis can also be performed in a SOEC. This reaction leads to the production of oxygen at the air electrode and carbon monoxide at the fuel electrode. Carbon monoxide is an important reagent. Incorporating CO into organic substrates can create higher value products, such as alcohols or esters.<sup>[7]</sup>

Since attention has always been focused on co-electrolysis, the CO<sub>2</sub> electrolysis has not been comprehensively studied yet. This work intends to examine the impact of CO<sub>2</sub>/CO ratio and different reaction temperatures on the underlying reactions and processes.

## 2 Theoretical Background

### 2.1 High-Temperature Electrolysis of CO<sub>2</sub> using SOECs

In this work the high temperature electrolysis of CO<sub>2</sub> was examined using SOECs, which are based on 8 mol-% yttrium oxide stabilized zirconium oxide (8YSZ). The electrodes are made of porous structures and are electronically conducting. These are important features to provide a sufficient gas transport to the electrolytically active triple-phase boundary. The cathode is a Ni/8YSZ cermet, which is generated from NiO/8YSZ by gradually introducing H<sub>2</sub> during the cell starting period. For the anode, a strontium doped lanthanum cobalt ferrite (LSCF) is used. The electrodes are separated by a dense, gas-tight solid electrolyte to prevent the burning of fuel components. This thin layer of electrolyte is based on 8YSZ, which is electronically insulating and solely oxygen ion conducting. Between the electrolyte and the air electrode, a gadolinium-doped ceria (GDC) barrier layer is applied. The total system can be written as: Ni-8YSZ/8YSZ/GDC/LSCF.

The high temperature electrolysis of CO<sub>2</sub> involves the reduction of CO<sub>2</sub> to CO and the diffusion of the generated oxygen ions (eq. 1) at the cathode. The ions will diffuse through the 8YSZ electrolyte to a triple-phase boundary at the anode site, followed by the oxidation of the oxygen ions to produce oxygen molecules (eq. 2):



The overall reaction of CO<sub>2</sub> electrolysis (eq. 3) is an endothermic process, which means from a thermodynamic point of view, that operation at high temperatures is advantageous.<sup>[8,9]</sup>



The total theoretical energy required for the CO<sub>2</sub> electrolysis is the amount of energy determined by the change in process enthalpy  $\Delta H$ . The enthalpy change is the sum of electrical and thermal energy,

$$\Delta H = \Delta G + T\Delta S, \quad (4)$$

where  $T\Delta S$  is the thermal energy demand and  $\Delta G$  the change in the Gibbs free energy. The latter is related to the minimum (reversible) cell voltage  $E_0$  (eq. 5), at which the reaction occur.<sup>[10]</sup>

$$E_0 = \frac{\Delta G(T)}{nF} \quad (5)$$

Here,  $n$  is the number of electrons transferred and  $F$  the Faraday's constant (96,485 C mol<sup>-1</sup>). For temperatures between 800 K and 1200 K, the reversible cell voltage  $E_0$  can be approximately calculated as

$$E_0 = 1.1043 - 0.00045(T - 800).^{[11]} \quad (6)$$

Figure 1 illustrates the temperature dependence of the energy demands for the H<sub>2</sub>O and CO<sub>2</sub> electrolysis. As indicated in this figure, increasing temperature has no significant impact on  $\Delta H$ , since this thermodynamic property remains approximately constant. However, increasing the operating temperature leads to a sharp decrease of  $\Delta G$ . Operating at high temperatures is therefore efficient, since the total energy demand is mostly provided by thermal energy.<sup>[5]</sup>

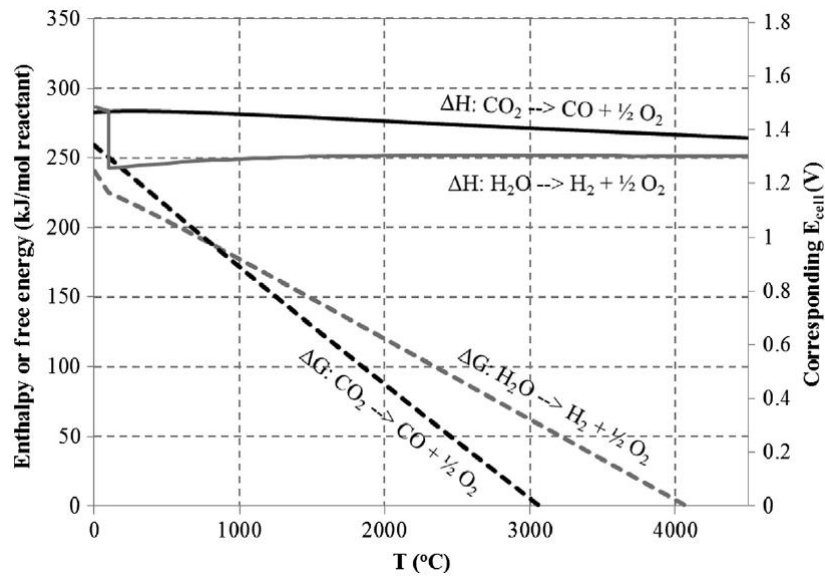


Figure 1: Enthalpy and free energy for the electrolysis of H<sub>2</sub>O and CO<sub>2</sub>.<sup>[5]</sup>

An important issue, which has to be considered, is the subsequent oxidation of the Ni electrode by pure CO<sub>2</sub>. Avoiding the deactivation of Ni can be achieved by ensuring a sufficient amount of H<sub>2</sub> or CO in the CO<sub>2</sub> feed. This will provide a reducing atmosphere over all parts of the electrode.<sup>[12]</sup>

However, a main challenge of the CO<sub>2</sub> electrolysis with CO remains the carbon deposition on the active sites of the Ni surface or within the porous electrode. This results in the deterioration of the electrochemical performance and the CO<sub>2</sub> conversion efficiency.<sup>[9]</sup> This effect become significant with decreasing temperature and is attributed to the catalytic effect of Ni for the Boudouard equilibrium:



Carbon monoxide containing gases are catalyzed to disproportionate into CO<sub>2</sub> and carbon. The coke formation is especially favored at high CO concentrations and low temperatures during CO<sub>2</sub> electrolysis, but can be shifted towards CO, when realistic CO/CO<sub>2</sub> concentrations are used for the electrolysis.<sup>[12,13]</sup>

## 2.2 Electrochemical Basics

### 2.2.1 Open Cell Voltage

The open cell voltage (OCV) occurs, when a cell is not connected to a consumer and an electrochemical equilibrium state is achieved. Under open circuit conditions no net processes occur, and the external current is zero. At ideal conditions, the OCV and the Nernst voltage are identical. However, ideal conditions are barely achieved and due to small leakages, the gas composition changes, leading to a different Nernst voltage which does not equal the theoretical OCV.<sup>[5]</sup> The Nernst voltage can be calculated according to the following equation:

$$E_N = E^0 + \frac{RT}{nF} \ln \left( \frac{p_{\text{CO}} \sqrt{p_{\text{O}_2}}}{p_{\text{CO}_2}} \right) \quad (8)$$

where  $E^0$  is the standard cell voltage,  $F$  the Faraday's constant,  $R$  the ideal gas constant ( $8.3145 \text{ J mol}^{-1} \text{ K}^{-1}$ ),  $T$  the operating temperature and  $p$  the partial pressure of the specific gases at the electrode surface.<sup>[11]</sup>

### 2.2.2 Polarization Processes

When current flows through an electrolysis cell, a higher voltage compared to OCV is obtained. This observation is attributed to polarization losses, which primarily originate from ohmic, concentration and activation polarization. The theoretically needed cell potential is caused by these polarization processes, which is a function of the current density.



1. Ohmic polarization (ohmic loss):

This type of voltage loss is due to the resistance to the movement of electric charge. The main contribution is provided by the oxide ion transport through the electrolyte. Besides the electrolyte contribution, the ohmic loss also includes the electron transfer through the electrodes and any contact resistances. In general, it can be described as shown in eq. 8:

$$E_{\text{ohm}} = I \sum_n R_n \quad (9)$$

Here,  $I$  denotes the current and  $R_n$  the resistances of all components that contribute to the ohmic loss.<sup>[5]</sup>

2. Concentration polarization:

The concentration polarization is related to an undersupply of gas at the reactive sites and can be divided into conversion polarization and diffusion polarization. The latter is caused by the resistance that arises from the gas transport through the pores of the electrode and can occur at the anode as well as the cathode. The conversion polarization is attributed to changes in the gas composition at the active electrode.

3. Activation Polarization:

Since electrode reactions involve charge transfer at the triple-phase boundary as a fundamental step, a certain energy barrier has to be exceeded. This energy demand causes a voltage loss, which is known as activation polarization.<sup>[5]</sup>

## 2.3 Electrochemical Characterization

### 2.3.1 $i/V$ Characterization

The current-voltage ( $i/V$ ) characterization is a method to assess the performance of SOECs using direct current (DC). It shows the relationship between the applied potential, which is changed stepwise, and the current flowing through the circuit.  $i/V$  curves are generally used as a tool to determine the area specific resistance (ASR). The ASR at low current densities and negligible polarization effects can be approximated using eq. 8,

$$ASR = \frac{E_{op} - E_{OCV}}{i} \quad (10)$$

where  $E_{op}$  is the operating voltage,  $E_{OCV}$  the open circuit voltage and  $i$  the current density.<sup>[5]</sup> However, in the scope of this work, the ASR was obtained by numerical derivation with python, since this method also allows the determination of the ASR at higher current densities.

### 2.3.2 Electrochemical Impedance Spectroscopy (EIS)

#### 2.3.2.1 Fundamentals

Electrochemical impedance spectroscopy (EIS) is a powerful method for analyzing electrical properties of materials. It is used for example for determining capacitances, resistances and kinetics of processes. A certain frequency of an AC source is applied, and the cell response is measured as a function of the applied frequency. This method enables the identification of the various polarizations, since they have different time dependencies.

EIS relies on a simple concept, in which impedance can be described as a complex resistance. Electrical resistance  $R$  is defined as the ratio between input voltage  $E_{in}$  and output current  $i_{out}$ , as it is described by Ohm's Law:<sup>[14]</sup>

$$R = \frac{E_{in}}{i_{out}} \quad (11)$$

However, this relationship is limited to an ideal resistor, which is independent of the AC frequency. The AC voltage and current signals will be in phase with each other. In comparison, impedance is also the ratio between voltage and current, but also takes the phase differences between the input voltage and output current into account. The applied voltage signal  $E(t)$ , involving the frequency  $f$ , can be expressed as a function of time  $t$ :<sup>[14]</sup>

$$E(t) = E_A \sin(2\pi ft) = E_A \sin(\omega t) \quad (12)$$

The resulting current response in a (pseudo)linear system to a sinusoidal voltage input is also sinusoidal but shifted in phase ( $\phi$ ):

$$I(t) = I_A \sin(\omega t + \phi) \quad (13)$$

The phase difference  $\phi$  is zero for purely resistive behavior and the impedance is completely frequency independent. Analogous to Ohm's Law, these expressions can be used to calculate the complex impedance of the system:<sup>[14,15]</sup>

$$Z^* = \frac{E(t)}{I(t)} = \frac{E_A \sin(\omega t)}{I_A \sin(\omega t + \phi)} = Z_A \frac{\sin(\omega t)}{\sin(\omega t + \phi)}. \quad (14)$$

Using Euler's relationship

$$e^{i\phi} = \cos(\phi) + i \sin(\phi), \quad (15)$$

the impedance can be expressed as a complex number, that contains a real part  $Z'$  and an imaginary part  $Z''$ :<sup>[14,15]</sup>

$$Z^* = \frac{E(t)}{I(t)} = \frac{E_A e^{i\omega t}}{I_A e^{i\omega t - i\phi}} = Z_A e^{i\phi} = Z_A (\cos(\phi) + i \sin(\phi)) = Z' + i Z''. \quad (16)$$

#### 2.3.2.2 Data Presentation

Impedance measurements produce data, which consists of the real part  $Z'$  and imaginary part  $Z''$ , as well as the frequency. There are several possibilities to present the data, which can be divided into two fundamental types of graphs:

##### 1. Nyquist Plots:

These types of plots are complex plane plots, which show the imaginary versus the real impedance part for decreasing frequencies. It is a very convenient and informative way of representing the data, since the shape of the curves and domains yield insight into possible kinetic phenomena and can be related to electrical equivalent circuit elements.

##### 2. Bode Plots:

The frequency dependent presentation of the impedance data is referred to as Bode plot. The absolute value  $|Z_A|$  or the phase shift  $\phi$  are plotted against the frequency on a logarithmic scale. An advantage of Bode plots, compared to Nyquist plots is, that the impedance behavior at high frequencies is shown with equal weight along the plot.<sup>[16]</sup>

### 2.3.2.3 Kramers-Kronig Test

The data quality can be validated using the Kramers-Kronig transformation. A requirement for this test is the application of a sinusoidal excitation, resulting in a linear response of the system over a wide range of frequencies.<sup>[17]</sup> The transformation allows the calculation of the imaginary part from the real component and vice versa. If the results of the transformation are consistent with the experimental obtained data, then the measurement can be stated as trustworthy. The validated data can be evaluated by fitting an equivalent circuit.<sup>[14,15]</sup>

### 2.3.2.4 Elementary Analysis

In order to interpret impedance data, equivalent electrical circuit models are used. An equivalent electrical circuit (EC) model, made up of different circuit elements, is fitted to the EIS data. The combination of physical, chemical and electrical components in electrical terms, is an attempt to represent a complex phenomenon. Within the scope of this work, only the most common and relevant circuit elements will be discussed. Common ideal circuit elements are resistors (R), capacitors (C) and inductors (L):

$$Z_R = R \quad (17)$$

$$Z_C = \frac{1}{i\omega C} \quad (18)$$

$$Z_L = i\omega L \quad (19)$$

In many cases, ideal circuit elements are not suitable for describing real systems. They require different nonideal circuit elements, such as the constant phase element (CPE or Q). Due to the distribution of relaxation times, an ideal capacitor, which has a single well-defined resonance frequency, is not suitable. A common element combining R and Q is the RQ element. In a Nyquist plot, it shows an upward half circle. Mathematically it can be described as:

$$Z_{RQ} = \frac{1}{\frac{1}{R} + (i\omega)^\alpha Q} \quad (20)$$

According to the Kirchhoff's law, the resistance R and the constant phase element can be combined as it is shown in eq. 18. For an exponent  $\alpha = 1$  and  $Q = C$ , the impedance of an RC element is described.<sup>[15]</sup>

### 2.3.2.5 Distribution of Relaxation Times

The evaluation of the measured EIS data by fitting against an equivalent circuit model oftentimes requires a good knowledge about the processes of the investigated electrochemical system.<sup>[18]</sup> This method is further limited, since in some cases suitable ECs may not exist or the system may be described by multiple models which provide fits of analogous quality.<sup>[14]</sup> In this regard, a technique facilitating an analysis without any a priori knowledge about the system can act as an useful alternative for interpreting EIS data. One approach is the Distribution of Relaxation Times (DRT). In this method, the characteristic distribution of typical timescales are identified by separating polarization processes with different time constants directly from the experimental EIS data.<sup>[19]</sup>

The impedance for the  $k$ th RC element in a series connection can be expressed by

$$Z_{\text{pol}}(f) = \frac{R_k}{1 + i2\pi f\tau_k} \quad (21)$$

where  $\tau_k = R_k C_k$  is the relaxation time of the  $k$ th RC circuit element. For an infinite number of RC elements, the continuous distribution function of relaxation times  $\gamma(\tau)$  can be introduced:

$$Z_{\text{pol}}(f) = \int_0^\infty \frac{\gamma(\tau)}{1 + i2\pi f\tau} d\tau \quad (22)$$

Since the determination of  $\gamma(\tau)$  is known to be an ill-posed mathematical problem, different approaches, such as the Tikhonov regularization are used. By plotting  $\gamma(\tau)$  against the relaxation time  $\tau$ , DRT plots, as shown in Figure 2 are obtained.\*

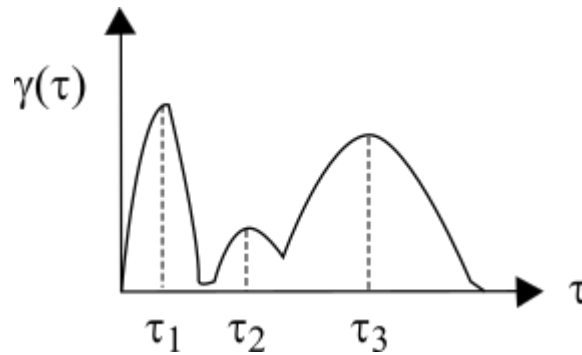


Figure 2: Schematic representation of a DRT plot.\*

---

\* Own illustration.

The representation of the EIS data in a DRT plot shows the distribution of time constants with characteristic shapes, widths and areas, where the enclosed areas are related to the different polarization resistances.<sup>[13,20]</sup>

### 3 State of the Art

Only limited studies have been reported for the dry CO<sub>2</sub> electrolysis, since the co-electrolysis gained high attention.

The first high temperature electrolysis of CO<sub>2</sub> was initiated by NASA. The electrolysis was performed in a SOEC over Pt and Ni cermet electrodes, aiming for an efficient O<sub>2</sub> generation for a long-term human exploration of the Mars. The production of O<sub>2</sub> from a mixture of CO<sub>2</sub>/CO leads to the formation of CO, which was treated as a side product. Using a Fe catalyst, the undesired CO was converted into CO<sub>2</sub> and carbon, according to the Boudouard equilibrium (eq. 6) and the new CO<sub>2</sub> was returned back to the main gas feed.<sup>[9,10]</sup>

In the early 1990s Ceramtec investigated the feasibility of SOFC button cells for electrolyzing a gas mixture of CO<sub>2</sub>/CO and H<sub>2</sub>/H<sub>2</sub>O.<sup>[5]</sup> It was shown that the ASR for CO<sub>2</sub>/CO was 10 times higher than that for the water electrolysis. However, over the past years the performance of the electrode materials were developed, yielding only about 100 – 200 % greater ASR.<sup>[5,21]</sup>

The dry CO<sub>2</sub> electrolysis was studied employing different cathode materials. The state-of-the-art material is Ni/YSZ. In 2009, it was shown that Ni/YSZ electrode supported SOECs are suitable for long term CO<sub>2</sub> electrolysis.<sup>[9]</sup> A passivation was observed, which was independent of coke formation but related to the site specific adsorption of sulphur from the gas feed. Activation of the deactivated Ni sites were achieved by carrying hydrogen to form volatile compounds such as H<sub>2</sub>S.<sup>[9]</sup> An alternative electrode material is La<sub>0.8</sub>Sr<sub>0.2</sub>Cr<sub>0.5</sub>Mn<sub>0.5</sub>O<sub>3</sub> (LSCM), infiltrated into a yttria-stabilized zirconia scaffold with 0.5 wt%. Pd supported on 5 wt% Ce<sub>0.48</sub>Zr<sub>0.48</sub>Y<sub>0.04</sub>O<sub>2</sub>. In comparison to the Ni/YSZ, this material benefits from being redox stable, not forming volatile carbonyl compounds and not being a good catalyst for the Boudouard reaction.<sup>[12]</sup> Another promising cathode material is GDC on YSZ electrolyte, which shows a significantly lower ASR for CO to CO<sub>2</sub> exchange than porous platinum and Ni/YSZ electrodes.<sup>[22]</sup>

Jensen et al. studied the performance of a cell composed of Ni-YSZ/YSZ/LSM-YSZ for the dry CO<sub>2</sub> electrolysis.<sup>[23]</sup> For a gas mixture of 70 % CO<sub>2</sub> and 30 % CO, a current density of 1.5 A cm<sup>-2</sup> and 21 % CO<sub>2</sub> utilization was obtained at 1.29 V and 950 °C. Furthermore, the performance was compared with the steam electrolysis and it was found out, that the internal resistance for the CO<sub>2</sub> electrolysis was 65 % higher under similar conditions. ASR values for

12

different CO<sub>2</sub>/CO composition were tested by Ebbesen and Mogensen.<sup>[9]</sup> They utilized similar cells with an active area of 16 cm<sup>2</sup> and obtained for a mixture of 50 % CO<sub>2</sub> and 50 % CO an ASR value of 0.36 Ω cm<sup>2</sup>. For 70 % CO<sub>2</sub> and 30 % CO a slightly higher ASR was obtained (0.37 Ω cm<sup>2</sup>). It was also reported, that these ASR values are higher, when operating in the fuel cell mode.<sup>[9]</sup>



## 4 Experimental

### 4.1 Setup

A 2-electrode setup with the Potentiostat Vertex.5A by Ivium Technologies was used to perform the measurements of the cathode-supported full-cells. The full-cell was sealed with a gold ring and mounted on top of the inner Pt-current collector, which is located above the air inlet. After fixing the cell, the second current collector made of Ni/Pt was placed on the fuel side. Stabilization of the full setup was ensured by fixing the complete sample holder with a spring-loaded lock. The fixed sample holder was closed with a ceramic housing, which additionally was equipped with a metal grid to shield the measurements from electrochemical disturbances.



Figure 3: Measurement setup for disk samples.<sup>[24]</sup>

### 4.2 Full-Cell

As described in the previous section, 8YSZ based full-cells were used. The total system can be expressed as Ni-8YSZ/8YSZ/GDC/LSCF. The cell diameter was 2 cm with an active area of 0.785 cm<sup>2</sup>.

### 4.3 Reduction of NiO

After installation of the setup, the cell was heated up to 900 °C, while 6 l·h<sup>-1</sup> compressed air was provided on the anode and 6 l·h<sup>-1</sup> nitrogen on the fuel side. The active Ni-YSZ cathode was generated by gradually reducing NiO with H<sub>2</sub> at 896 °C (see Table 1). During the reduction process, the OCV was monitored. With increasing reduction step, the potential was increasing. After reaching a constant value, the composition of the gas mixture was adjusted to the next step.

Table 1: Reduction steps.

$\dot{V}_{H_2} / \text{l} \cdot \text{h}^{-1}$	$\dot{V}_{N_2} / \text{l} \cdot \text{h}^{-1}$	$\dot{V}_{\text{air}} / \text{l} \cdot \text{h}^{-1}$
-	6	6
0.5	6	6,5
1	6	7
2	6	8
3	6	9
4	5	9
5	4	9
6	3	9
7	2	9
8	1	9
9	-	9

#### 4.4 Electrochemical Measurements

##### i/V Characterization

After completing the reduction of NiO, i/V and EIS measurements were conducted at varying gas mixtures and temperatures. Throughout the work the gas flow of each reaction side was kept at  $6 \text{ l} \cdot \text{h}^{-1}$  and compressed air was introduced to the anode. The cell performance was tested by measuring the i/V-curves from OCV to 1.4 V with a scan rate of  $0.01 \text{ A s}^{-1}$ . Comparability among different cells was achieved by a normalization procedure. For this procedure, an i/V curve starting from OCV to 0.6 V with  $H_2$  on the fuel side and air at the anode side was measured with a scan rate of  $10 \text{ A s}^{-1}$  in the fuel cell mode. The real contacted area was determined by dividing the current value for 0.6 V by the ideal current density for 100 % contact, which was  $3 \text{ A cm}^{-2}$ .<sup>[25]</sup>

##### EIS Characterization

The EIS measurements were conducted at various conditions. The frequency for the measurements was ranging from 11100 Hz to 0.11 Hz resulting in approx. 64 data points. The measurement series started at the OCV, and the current density was increased stepwise by  $25 \text{ mA cm}^{-2}$  until  $400 \text{ mA cm}^{-2}$  was reached. Depending on the previously measured i/V-curves, higher current densities were measured, whereby the current density was increased stepwise by  $50 \text{ mA cm}^{-2}$ .

Two different gas mixtures with CO<sub>2</sub>:CO ratios of 4:1 and 1:1 were investigated. The varying parameters for these mixtures are listed in Table 2.

Table 2: Experiment parameters.

CO <sub>2</sub> /CO	Varied Parameter	Variation
80/20	Temperature / °C	698, 713, 732, 749, 768, 786, 809, 828, 851, 874, 900
50/50	Temperature / °C	700, 811, 901
50/50, 80/20	(EIS) Current Density / mA cm <sup>-2</sup>	0 – 400 in 25 mA cm <sup>-2</sup> steps 450 – 900 in 50 mA cm <sup>-2</sup> steps

## 5 Results and Discussion

### 5.1 i/V Curves

In order to gain information about the impact of the reaction temperature and gas mixture on the performance of the SOEC, i/V measurements were conducted. The obtained data can be used to determine the open circuit voltage (OCV) and the area specific resistance (ASR). The latter is equal to the slope of the i/V curve at a desired current density. In this work, the ASR was calculated for  $0.1 \text{ A cm}^{-2}$ . Furthermore, the current density  $i_{1.4 \text{ V}}$  at our chosen maximum of 1.4 V can be obtained, which gives insight into the performance of the cell. This maximum voltage was chosen, in order to keep degradation and aging effects which might occur at higher voltages, as low as possible.

Figure 4 shows the i/V curves in different  $\text{CO}_2:\text{CO}$  mixtures ( $\text{CO}_2:\text{CO} = 80:20$  and  $50:50$ ) recorded at temperatures in the range of 698 – 901 °C. This figure reveals that the performance is highly dependent on the temperature as well as the composition of the gas mixture. Upon increasing the temperature, the curves exhibit two sections with different slopes. Slightly higher slopes can be found at higher current densities. This observation might be due to diffusion polarization, since applying high current densities will result in a high  $\text{CO}_2$  consumption. If the subsequent delivery of the reactant is not fast enough, a  $\text{CO}_2$  depletion at the cathode will result in a higher resistance.

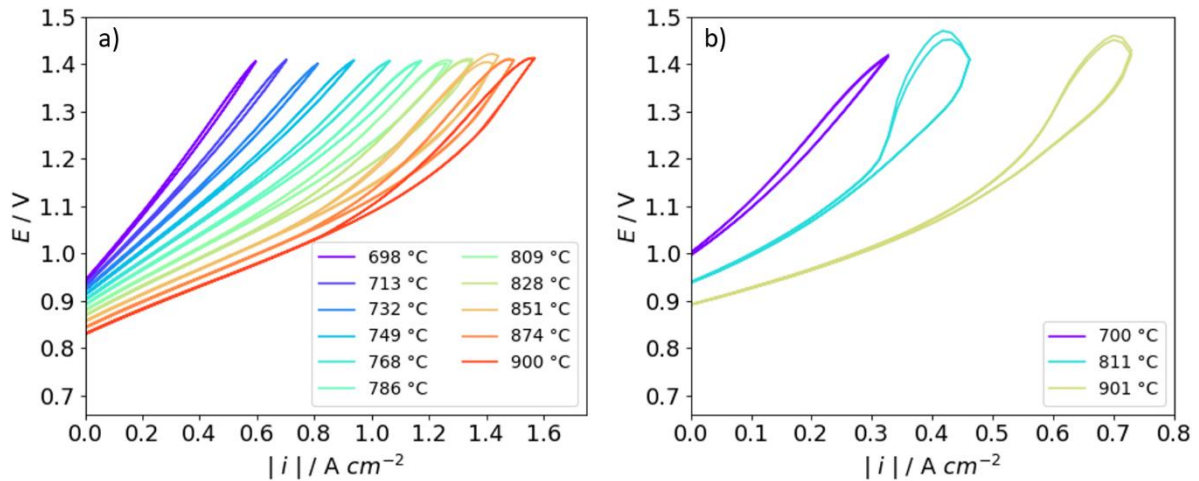


Figure 4: i/V curves at different temperatures; a) 80 %  $\text{CO}_2$ , 20 %  $\text{CO}$ , b) 50 %  $\text{CO}_2$ , 50 %  $\text{CO}$ .

Increasing the temperature also leads to a hysteresis of the i/V curves. For a mixture of 80:20  $\text{CO}_2:\text{CO}$ , the hysteresis becomes more significant with each increasing temperature step. At

temperatures higher than approx. 800 °C, no further increase was observed. Similar to the mixture with 80:20 CO<sub>2</sub>:CO, the hysteresis for 50:50 CO<sub>2</sub>:CO also grows with increasing temperature until approx. 811°C. The most probable reason for this behavior is the deterioration of the electrode due to sintering. However, for the CO<sub>2</sub>:CO ratio of 50:50, the hysteresis of the curves are much higher. This can likely be attributed to the higher CO amount, since the coke formation is preferred at high CO concentrations. Deposition of coke at the active sites, especially at the three phase boundary, where gaseous CO<sub>2</sub>, Ni and ionically conductive YSZ meet, will reduce the active electrode area. This will lead to an increased cell resistance, hence to a higher voltage in the i/V curve. In the following, the values for the OCV, ASR and  $i_{1.4\text{ V}}$ , were determined as described before and are summarized in Table 3.

Table 3: Measurement parameters: temperature (T), theoretical and experimental open circuit potential (OCV), area specific resistance (ASR) and current density at 1.4 V.

CO <sub>2</sub> /CO	T / °C	OCV <sub>theor</sub> / V	OCV <sub>exp</sub> / V	ASR / Ω cm <sup>2</sup>	i <sub>1.4 V</sub> / A cm <sup>-2</sup>
80/20	698	0.94	0.94	0.70	0.58
80/20	713	0.93	0.93	0.60	0.69
80/20	732	0.92	0.92	0.52	0.81
80/20	749	0.91	0.91	0.46	0.92
80/20	768	0.90	0.90	0.41	1.05
80/20	786	0.89	0.89	0.37	1.14
80/20	809	0.88	0.88	0.34	1.24
80/20	828	0.87	0.87	0.31	1.30
80/20	851	0.85	0.86	0.28	1.35
80/20	874	0.84	0.84	0.27	1.44
80/20	900	0.83	0.83	0.26	1.52
50/50	700	0.99	1.00	1.14	0.31
50/50	811	0.94	0.94	0.65	0.46
50/50	901	0.90	0.89	0.37	0.66

The experimental determined OCV is in agreement with the calculated values according to the Nernst equation. The results reveal that increasing temperature leads to decreasing OCV values, which is independent of the CO<sub>2</sub>:CO ratio. However, compared to the gas mixture with 80:20 CO<sub>2</sub>:CO, the mixture with a higher CO concentration shows slightly higher OCV values. These findings are consistent with the Nernst equation (eq. 7), since low potentials at high temperatures and high potentials for high CO amounts, are predicted.

The ASR is the total resistance of a cell, which gives information regarding the performance of a cell. High performances are achievable, if the ASR is low. It decreases with increasing temperature, as it can be seen from Figure 5. This is due to the fact, that at high temperatures these electrolysis processes are thermodynamically and kinetically favored. For 80:20 CO<sub>2</sub>:CO, an exponential decrease can be found. The ASR decreases slower than the temperature increases, which indicates different processes or an upper reaction temperature limit.

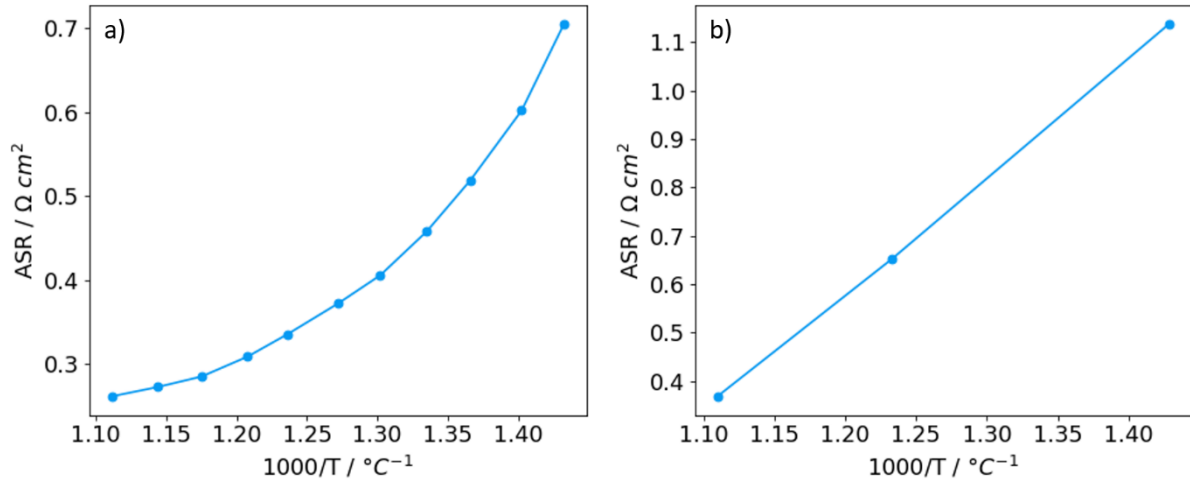


Figure 5: The area specific resistance (ASR) plotted against the reciprocal of the temperature for a) 80 % CO<sub>2</sub>, 20 % CO, b) 50 % CO<sub>2</sub>, 50 % CO.

In comparison to the gas mixture with 80 % CO<sub>2</sub>, the summarized results reveal a lower electrolysis efficiency for the mixture containing 50 % CO<sub>2</sub> and 50 % CO over the whole investigated temperature range. The values for the ASR are approximately twice of that for a mixture with 80 % CO<sub>2</sub> and 20 % CO. The higher ASR values for the gas mixture with 50 % CO<sub>2</sub> and 50 % CO might be attributed to the decreased total CO<sub>2</sub> content. Another reason for the higher ASR for 50 % CO might be the deterioration of the electrode due to coke formation, leading to a reduced active electrode area.

The maximum current density that can be achieved at 1.4 V, is increasing as the temperature rises, which is consistent with the obtained ASR values. For a gas mixture of 80:20 CO<sub>2</sub>:CO, the maximum normalized current density is 0.58 A cm<sup>-2</sup> at 698 °C and 1.52 A cm<sup>-2</sup> at 900 °C.

## 5.2 Impedance Spectroscopy

In order to gain a deeper insight into the processes and to find out, how these processes might be affected by temperature, current density and different atmospheres, EIS measurements were conducted at various conditions, as described in the previous section.

For successful validated experimental data according to the Kramers-Kronig relation, an equivalent circuit model, as shown in Figure 6 was developed. It consists of an inductance, a serial resistance, also known as ohmic resistance  $R_\Omega$ , and four RQ elements.

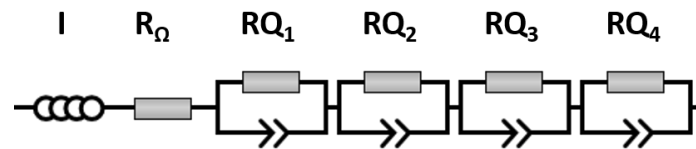


Figure 6: Equivalent circuit model for the high temperature electrolysis of  $\text{CO}_2$ .

The quality of the fit is determined by comparing the observed data from an EIS measurement to the hypothetical circuit model. If the fit matches the experimental data, and the residuals are not systematic, it is deemed to be a valid model.

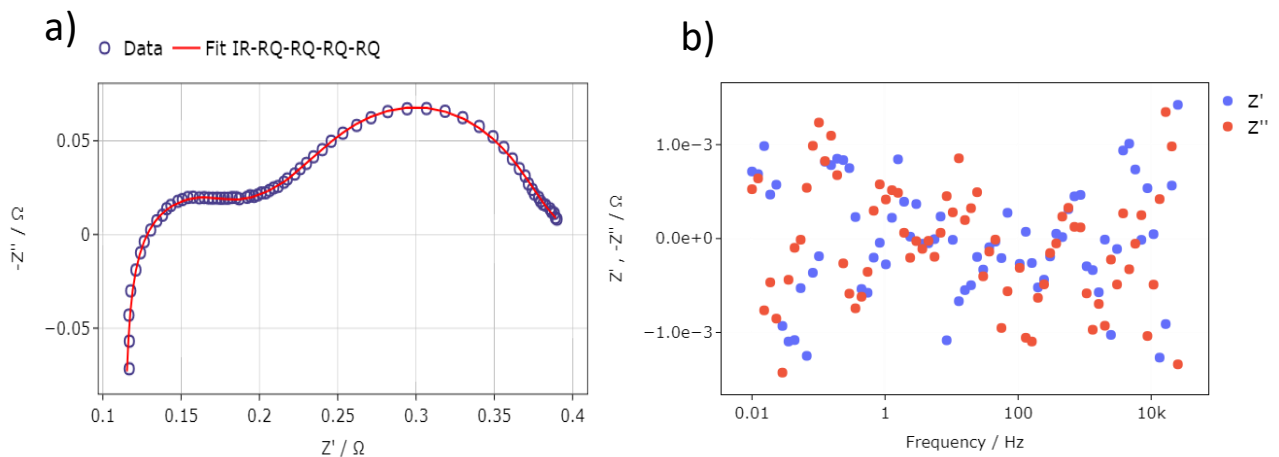


Figure 7: a) Experimental recorded EIS and calculated fit and b) residual analysis for electrolysis of 80%  $\text{CO}_2$  and 20%  $\text{CO}$  at 900 °C and 150  $\text{mAcm}^{-2}$ .

### 5.2.1 Temperature Dependence

Figure 8 shows the impedance spectra recorded in a 80:20 CO<sub>2</sub>:CO gas mixture at OCV and 0.35 A cm<sup>-2</sup> at different temperatures. As it can be seen, increasing temperature leads to a shift of the spectra to lower impedances and to a reduction of the number of the arcs. At 698 °C, three arcs were observed, whereas the number of distinctly visible arcs decrease to two at 900 °C. The results in Table 4 reveal, that the serial resistance is decreasing as the temperature is increasing. The serial resistance includes contribution of ohmic resistances of the contacts, electrode and electrolyte components. However, this finding reveals, that the ohmic contribution of the metals, such as Ni and Pd are negligible. Since the conductivity of ionic conductors are increasing with increasing temperature, this change in the serial resistance can be assigned to the contribution from the ionic conductors.

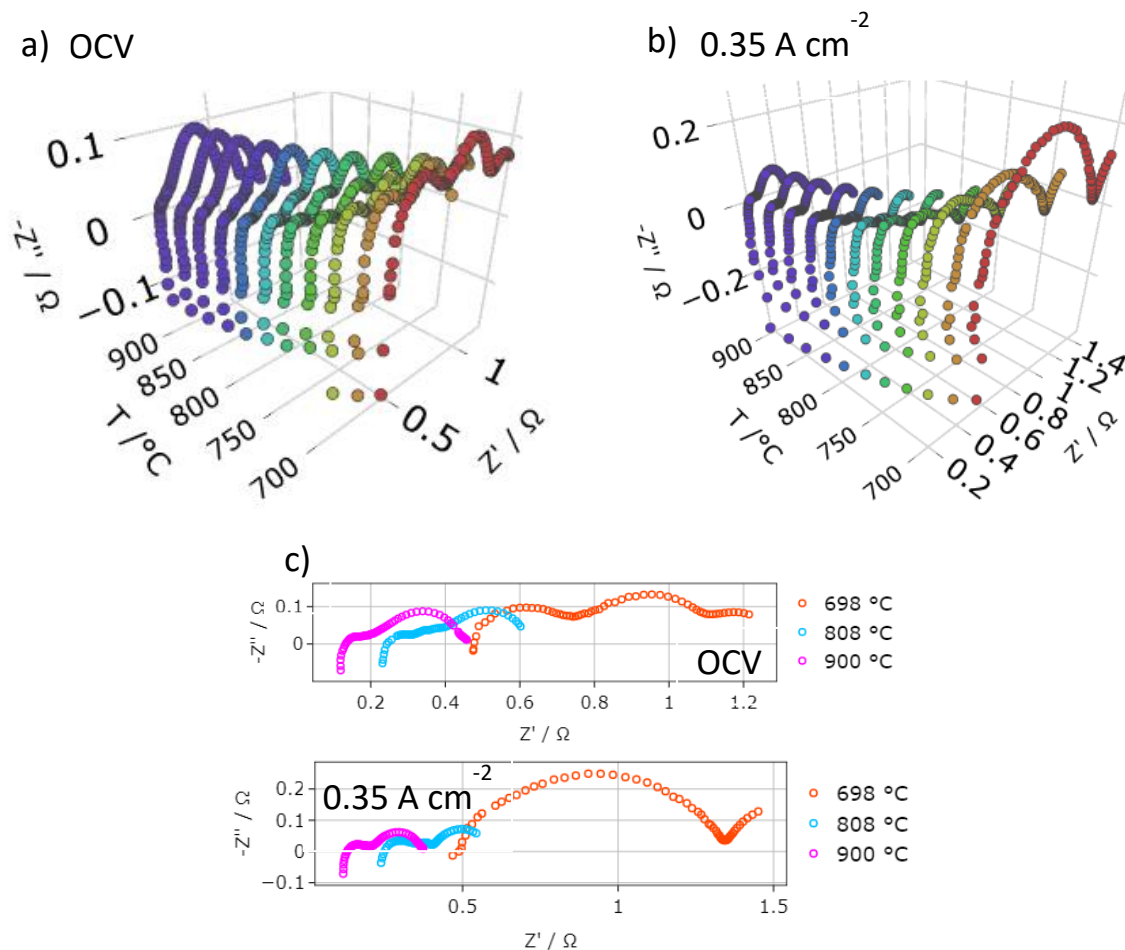


Figure 8: Nyquist plots of impedance spectra recorded during electrolysis of 80% CO<sub>2</sub> and 20% CO.



The polarization resistances are higher than the serial resistances, however they show a similar temperature dependency as the serial resistance. As a result of these behaviors, the total resistance is decreasing with increasing reaction temperature.

Table 4: Measuring temperature, total resistance ( $R_{tot}$ ) derived from EIS data, serial resistance ( $R_{\Omega}$ ), polarization resistance ( $R_{pol}$ ) and total resistance derived from the ASR values ( $R_{ASR}$ ). Measurement recorded at OCV in a mixture of 80%  $CO_2$  and 20%  $CO$

		OCV			0.35 A cm <sup>-2</sup>		
T/°C	$R_{ASR} / \Omega$	$R_{tot} / \Omega$	$R_{\Omega} / \Omega$	$R_{pol} / \Omega$	$R_{tot} / \Omega$	$R_{\Omega} / \Omega$	$R_{pol} / \Omega$
698	0.90	1.27	0.46	0.82	1.68	0.42	1.25
714	0.77	1.09	0.42	0.67	1.37	0.40	0.97
732	0.66	0.95	0.19	0.76	1.11	0.36	0.75
749	0.58	0.86	0.33	0.53	0.78	0.30	0.49
768	0.52	0.77	0.29	0.48	0.68	0.26	0.42
786	0.47	0.70	0.26	0.44	0.61	0.10	0.50
808	0.43	0.60	0.21	0.39	0.59	0.23	0.35
828	0.39	0.65	0.23	0.41	0.54	0.21	0.33
851	0.36	0.60	0.21	0.39	0.49	0.19	0.30
874	0.35	0.56	0.18	0.38	0.45	0.17	0.29
900	0.33	0.52	0.15	0.37	0.43	0.15	0.28

The spectrum in Figure 8 can be analyzed by fitting the developed model (see Figure 6) to the measured data. In this way the specific resistance contributions of each circuit element can be determined. According to the Arrhenius law, the resistance is related to the temperature according to the following equation

$$\ln R = -\ln A + \frac{E_A}{N_A k_B T} \quad (23)$$

where  $R$ ,  $T$ ,  $A$ ,  $E_A$ ,  $N_A$ ,  $k_B$  are the resistance, the temperature, the pre-exponential factor, the activation energy, the Avogadro and Boltzmann constant, respectively.

Plotting the logarithm of the resistance against the reciprocal temperature enables the calculation of the activation energy from the slope.

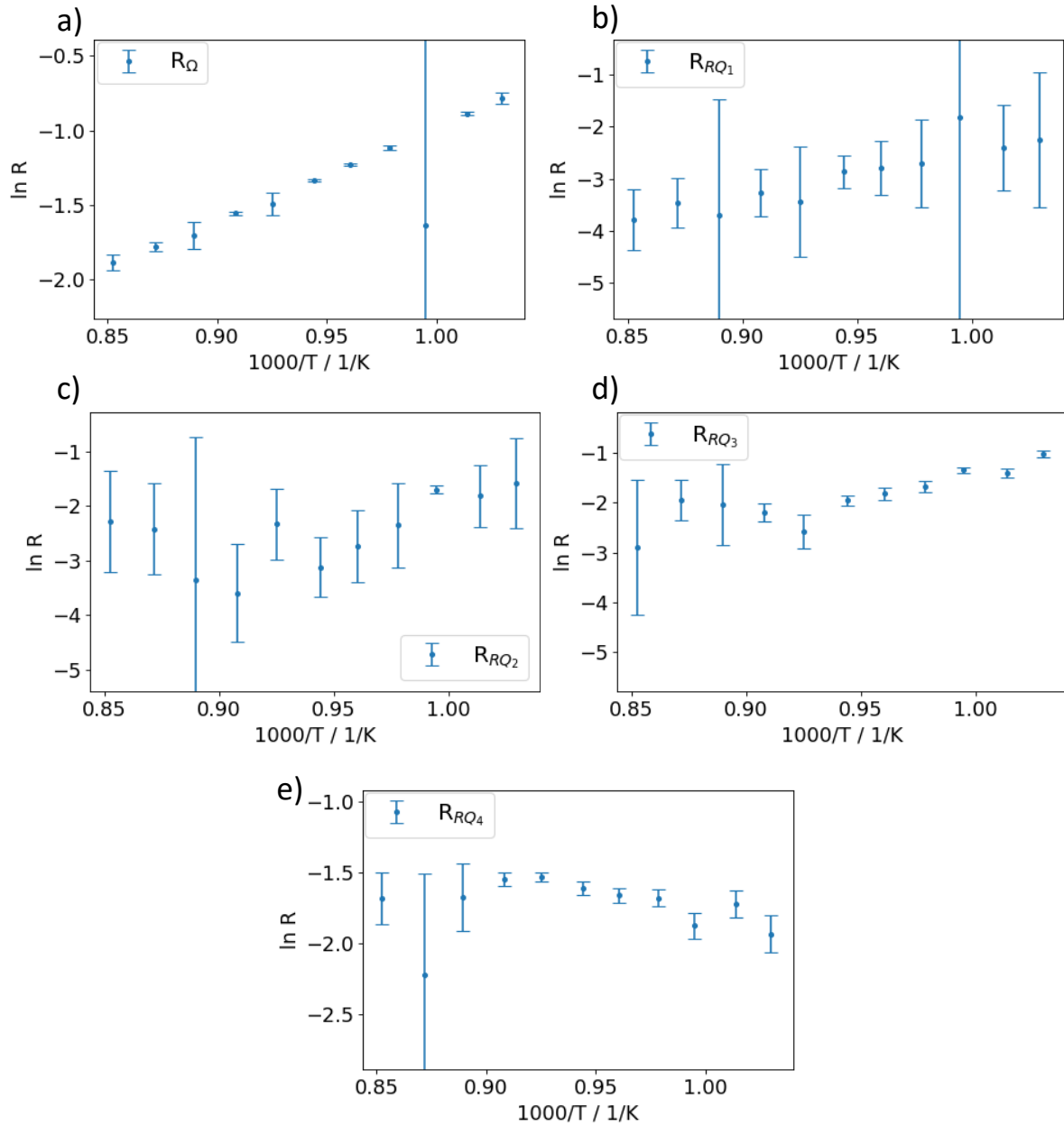


Figure 9: Natural logarithm of  $R_{\Omega}$ ,  $R_{RQ1}$ ,  $R_{RQ2}$ ,  $R_{RQ3}$  and  $R_{RQ4}$  against the reciprocal temperature. Measurement recorded at OCV in a mixture of 80%  $\text{CO}_2$  and 20%  $\text{CO}$ .

As can be seen from Figure 9, the plots for  $R_{\Omega}$  and  $R_{RQ1}$  exhibit apart from small deviations in the measured temperature range a nearly constant slope. The Arrhenius plots for  $R_{RQ2}$ ,  $R_{RQ3}$  and  $R_{RQ4}$  reveal that these resistances have temperature dependent activation energies, since the slopes are not constant. One reason for this observation might be, that the determined equivalent circuit model with four RQ elements is not suitable for describing this system. The

Arrhenius plots for the same gas mixture (80 % CO<sub>2</sub>, 20 % CO) recorded at 0.35 A cm<sup>-2</sup> are shown in Figure 10.

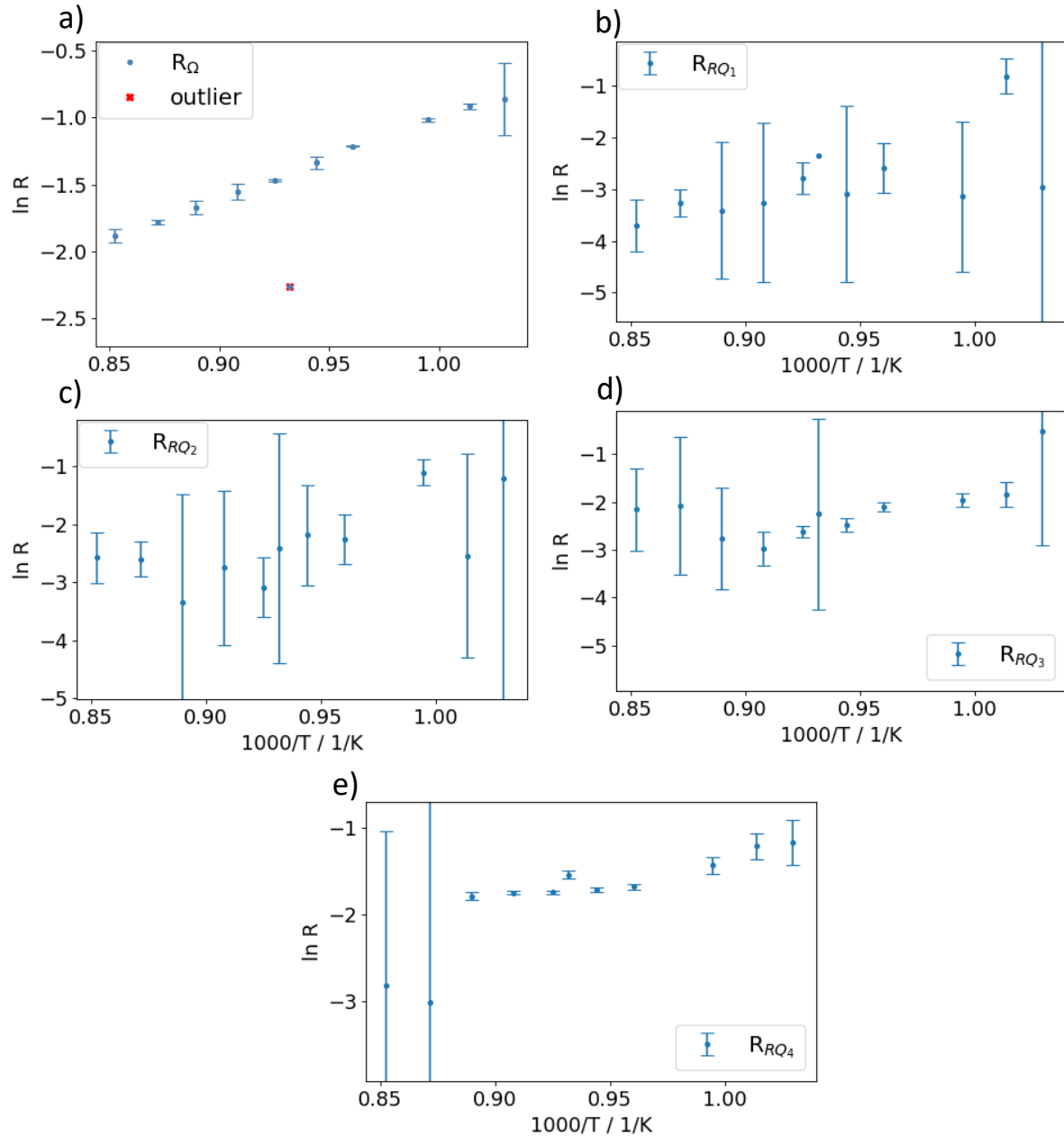


Figure 10: Natural logarithm of  $R_\Omega$ ,  $R_{RQ1}$ ,  $R_{RQ2}$ ,  $R_{RQ3}$  and  $R_{RQ4}$  against the reciprocal temperature. Measurement recorded at 0.35 A cm<sup>-2</sup> in a mixture of 80% CO<sub>2</sub> and 20% CO.

From Figure 10, it can be seen, that  $R_\Omega$  exhibit a constant slope over the measured temperature range (698 °C – 900 °C). The same behavior for  $R_\Omega$  was also found for measurements at OCV. However, for 0.35 A cm<sup>-2</sup>, no linear correlation between the reciprocal temperature and the natural logarithm of the four RQ-resistances ( $R_{RQ1-4}$ ) was observed. A slight temperature

independence of  $\ln R_{RQ4}$  was observed in the temperature range between 745 °C and 861 °C at 0.35 A cm<sup>-2</sup>, which indicates a small activation energy for this range.

In the following, the different slopes for different temperature ranges were not considered when calculating the activation energies according to Arrhenius law. Instead, an average activation energy for each element was determined (Table 5). Since this method contains errors and uncertainties, the ASR values determined in the previous section by i/V measurements, were plotted according to the Arrhenius equation (Figure 11).

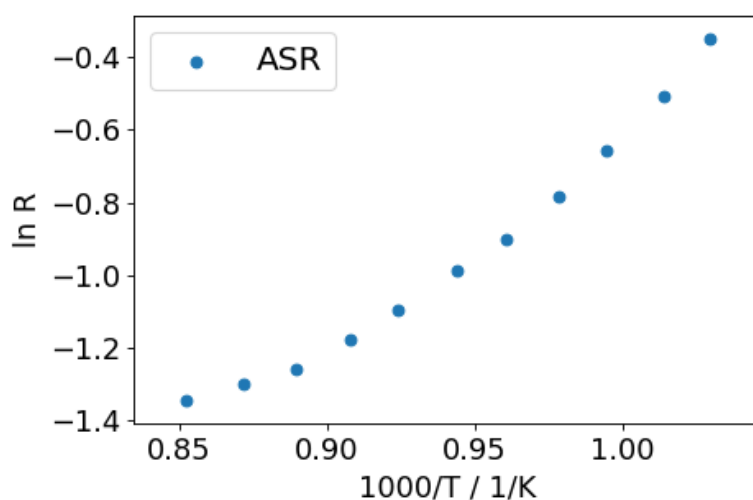


Figure 11: Natural logarithm of the ASR against the reciprocal temperature. Measurement recorded in a mixture of 80% CO<sub>2</sub> and 20% CO, the ASR was determined from i/V measurements at 0.1 A cm<sup>-2</sup> (chapter 2.3.1).

The Arrhenius plot of the ASR values shows a nearly linear correlation (Figure 11). This data can be used, to determine the activation energy from the slope. The results are summarized in Table 5.

Table 5: Calculated activation energies of the resistances in a 80 % CO<sub>2</sub> and 20% CO mixture. Values for OCV and 0.35 A cm<sup>-2</sup> were calculated using the EIS data, the result at 0.1 A cm<sup>-2</sup> was calculated using the ASR value determined from i/V measurements. R<sub>pol</sub> is the sum of the four RQ-resistances.

Parameter	E <sub>A</sub> / kJ mol <sup>-1</sup>		
	OCV	0.35 A cm <sup>-2</sup>	0.1 A cm <sup>-2</sup>
R <sub>Ω</sub>	52.4	49.4	
R <sub>RQ1</sub>	82.2	67.1	
R <sub>RQ2</sub>	54.2	68.0	
R <sub>RQ3</sub>	65.6	60.3	
R <sub>RQ4</sub>	-0.89	72.8	
R <sub>pol</sub>	201.2	268.2	
ASR	/	/	46.5

The calculated activation energy for R<sub>Ω</sub> at OCV is 52.4 kJ mol<sup>-1</sup>, which is slightly lower than the reported value of 75.1 kJ mol<sup>-1</sup> from a LSCM/GDC cathode in 70 % CO<sub>2</sub> and 30 % CO.<sup>[26]</sup> This difference might be due to different cell materials, since R<sub>Ω</sub> includes contribution of ohmic resistances from the contacts and the cell materials, such as the electrolyte and electrode. The calculated values for R<sub>RQ1</sub>, R<sub>RQ2</sub>, R<sub>RQ3</sub> and R<sub>RQ4</sub> at OCV are 82.2, 54.2, 65.6 and -0.89 kJ mol<sup>-1</sup>, respectively. In the above mentioned work, the equivalent circuit model determined for the electrolysis with a LSCM/GDC cathode consists of an inductor, followed by an serial resistance and two serial CPE. This indicates different polarization losses for this type of system, which might be attributed to different kinetics of the elementary reactions on the LSCM/GDC cathode. Furthermore, more than one model might exist, which could be used to describe a system. In this work, it was preferred to resolve the polarization resistances into four parts due to smaller residual values. However, comparing the polarization resistances shows, that the difference in the model might be due to different reaction kinetics. For the LSCM/GDC cathode a value of 75.1 kJ mol<sup>-1</sup> was reported, whereas the experimental determined value for R<sub>pol</sub> at OCV in this work is 201.2 kJ mol<sup>-1</sup>. In addition to different kinetics, the non-Arrhenius behavior of the four CPE elements was not considered, which have an influence on the result. Therefore, the ASR was used to calculate the activation energy, since the calculated values are model independent. The calculated activation energy from the ASR for CO<sub>2</sub>/CO 80/20 is 46.5 kJ mol<sup>-1</sup> and is about 20 % smaller than the reported value of 58.2 kJ mol<sup>-1</sup> for a

LSCM/GDC cathode in CO<sub>2</sub>/CO 70/30.<sup>[26]</sup> However, both values are in the same order of magnitude. The difference in the gas composition might have a negligible impact on the activation energy calculated from the ASR, since it was reported that no significant variation of the activation energy with different CO<sub>2</sub>/CO gas mixtures were observed when using gadolinia-doped ceria cathodes (GDC/YSZ/GDC).<sup>[22]</sup> For the GDC/YSZ/GDC system with CO/CO<sub>2</sub> ratios of 0.05, 0.25 and 0.5 an activation energy of ~100 kJ mol<sup>-1</sup> was reported.<sup>[22]</sup>

Besides the temperature dependence at OCV, the dependence at 0.35 A cm<sup>-2</sup> was analyzed. As it can be seen from Table 5,  $R_{\Omega}$  at OCV is 52.4 kJ mol<sup>-1</sup>, whereas it is 49.4 kJ mol<sup>-1</sup> at 0.35 A cm<sup>-2</sup>. The slight decrease might be related to the changes in  $R_{RQ}$ , affecting the intercept of the impedance spectra with the real axis at high frequency. The decreased value could also be attributed to the Joule heat effect and the p-type conduction in YSZ electrolytes.<sup>[27]</sup> The calculated activation energies for  $R_{RQ1}$ ,  $R_{RQ2}$ ,  $R_{RQ3}$  and  $R_{RQ4}$  are 67.1, 68.9, 60.3 and 72.8 kJ mol<sup>-1</sup>, respectively. The values for  $R_{RQ1}$  and  $R_{RQ2}$  decreased about 19 % and 8 % compared to the values at OCV, which indicates faster kinetics for these processes at load. The activation energies for  $R_{RQ2}$  and especially for  $R_{RQ4}$  increased significantly from 54.2 kJ mol<sup>-1</sup> to 68 kJ mol<sup>-1</sup> and from -0.89 kJ mol<sup>-1</sup> to 72 kJ mol<sup>-1</sup>, respectively.

Since the primary research focus to date has been the high-temperature co-electrolysis, limited studies have been reported for the electrolysis of dry CO<sub>2</sub>. No data under similar conditions could be found in the literature, therefore a comparison of the results and the assignment of the elements to processes is not possible.

A different approach to analyze the temperature dependence is by a 2-dimensional representation of the DRT in dependence of the temperature as shown in Figure 12.

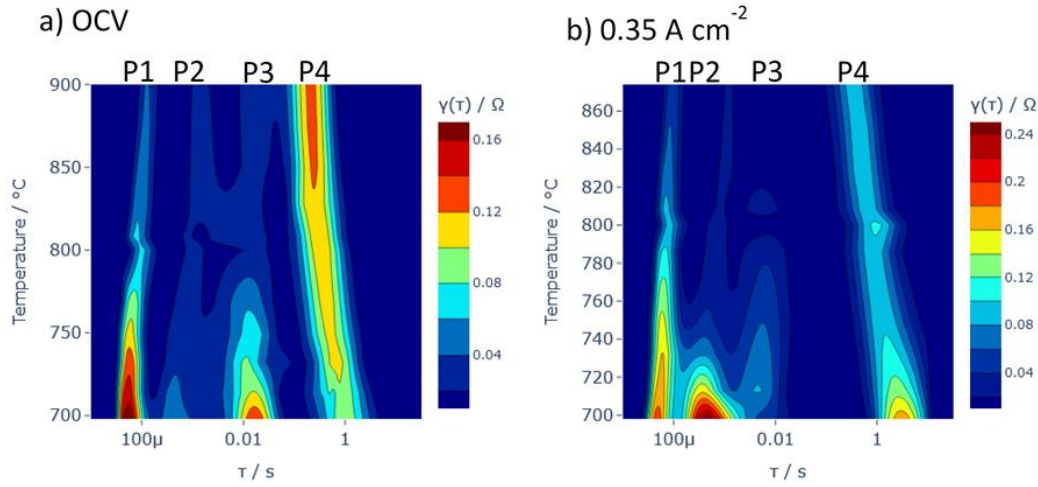


Figure 12: 2-D representation of the distribution of relaxation times (DRT) for different temperatures, where  $\gamma(\tau)$  is the distribution function and  $\tau$  the relaxation time. Electrolysis was conducted in a mixture of 80% CO<sub>2</sub> and 20% CO at 698, 808 and 900 °C.

Figure 12 reveals three main processes for the electrolysis at OCV and 0.35 A cm<sup>-2</sup>. The high frequency process P1 appears between the relaxation times of 35 μs – 90 μs (11111 Hz – 28571 Hz). Increasing temperature leads to a smaller distribution function  $\gamma(\tau)$  value of P1, which is current independent, since similar tendency of P1 can be seen at OCV and 0.35 A cm<sup>-2</sup>. The second process P2 can be found between 250 μs – 878 μs (1138 Hz – 4000 Hz). At OCV, P2 is a weak process with low intensity showing no temperature dependence. However at 0.35 A cm<sup>-2</sup>, the process gets more significant and the frequency range is getting broader. Furthermore, a temperature dependence can be seen, since the process starts with a high  $\gamma(\tau)$  value at 700 °C and diminishes with raising temperature. The third process P3 occurs at OCV between 0.005 s and 0.004 s (200 Hz – 250 Hz) and is one of the three main processes, which takes place at OCV. Similar to the last processes, the intensity of the distribution function is getting smaller with increasing temperature. Figure 12b reveals that P3 is not significantly contributing to the polarization resistance due to low  $\gamma(\tau)$  values. It can be seen, that at 0.35 A cm<sup>-2</sup> P3 is shifted to higher frequencies, which could have merged with P2 leading to broader P2 at 0.35 A cm<sup>-2</sup>. The last process P4 can be seen between 0.085 s and 2.02 s (0.50 Hz – 11.76 Hz). The temperature dependence of this process is current dependent, since at OCV the value for  $\gamma(\tau)$  increases, whereas at 0.35 A cm<sup>-2</sup>  $\gamma(\tau)$  decreases with increasing temperature. Furthermore, it can be seen, that the number of processes is decreasing with

increasing temperature. This finding, that only three main processes are visible in the DRT, are not consistent with the equivalent circuit model, since the model consists of four RQ elements. One possible reason might be, that the calculation of the DRT is an ill-posed problem. The calculation requires regularization methods, such as the Tikhonov regularization, which are strongly parameter dependent. Another reason might be, that the determined equivalent circuit model in Figure 6 provides a suitable fit with a good quality, even though it might not describe the occurring processes sufficiently. Furthermore, some processes in the DRT might be too weak to fit them precisely, which might lead to this inconsistency.

### 5.2.2 Current Density Dependence

The current dependence of the electrolysis with 80% CO<sub>2</sub> and 20% CO was investigated for the temperatures 698, 808 and 900 °C. Impedance measurements were conducted at different current densities, ranging from 0 – 950 A cm<sup>-2</sup> (see Figure 13).

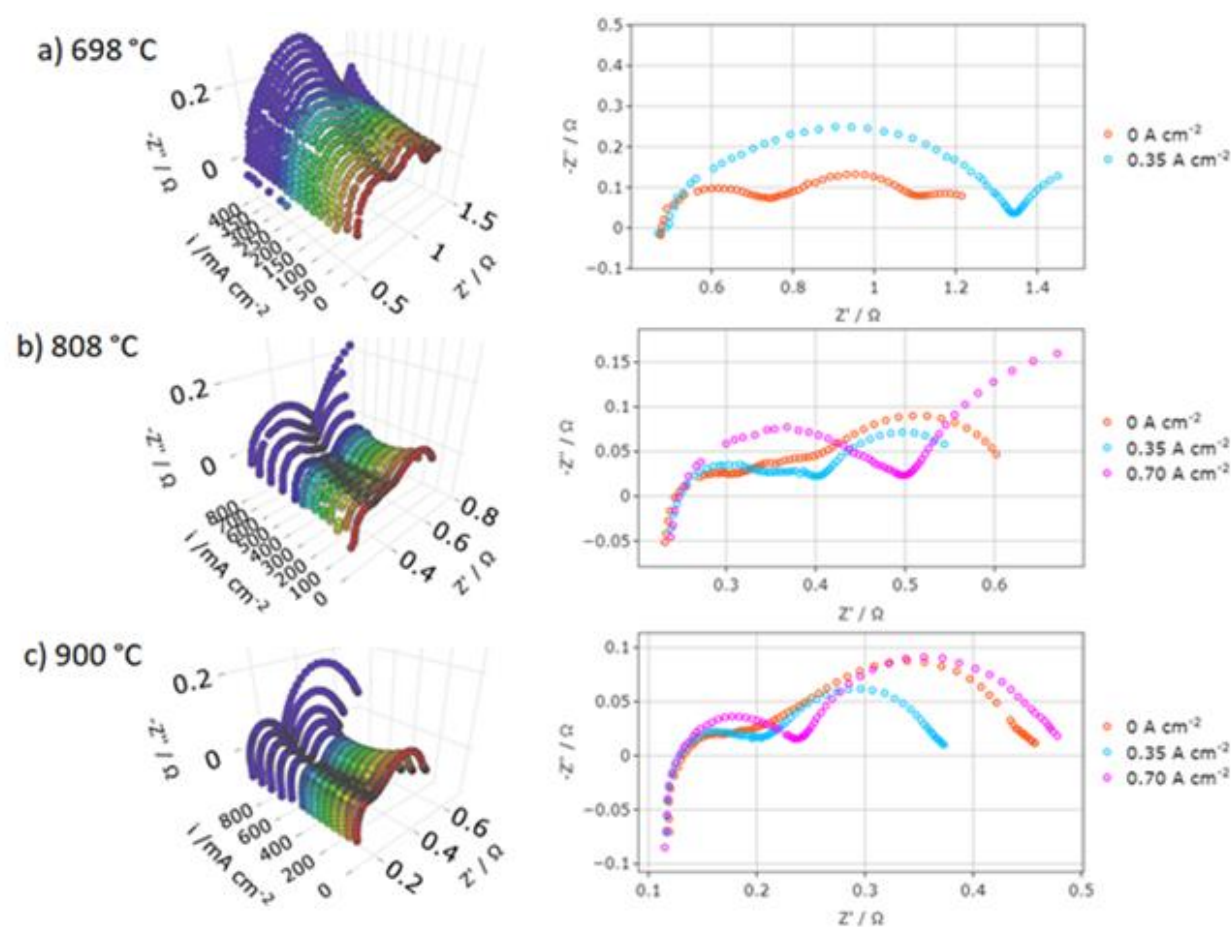


Figure 13: Nyquist plots of impedance spectra recorded during electrolysis of 80% CO<sub>2</sub> and 20% CO.



Figure 13 shows the EIS measured in 80% CO<sub>2</sub> and 20% CO under various current densities at three different temperatures. It can be clearly seen that the intercept of the spectra with the real axis at high frequency varies with temperature. However, it remains constant for varying current densities. Another observation is the tendency of increasing total resistance with increasing current density. In order to analyze, which processes are influenced by the current density, the spectra were fitted with the equivalent circuit model as shown in Figure 6. The obtained values for the serial resistance  $R_{\Omega}$ , polarization resistance  $R_{pol}$  and total resistance  $R_{tot}$  were plotted against the current density (see Figure 14).

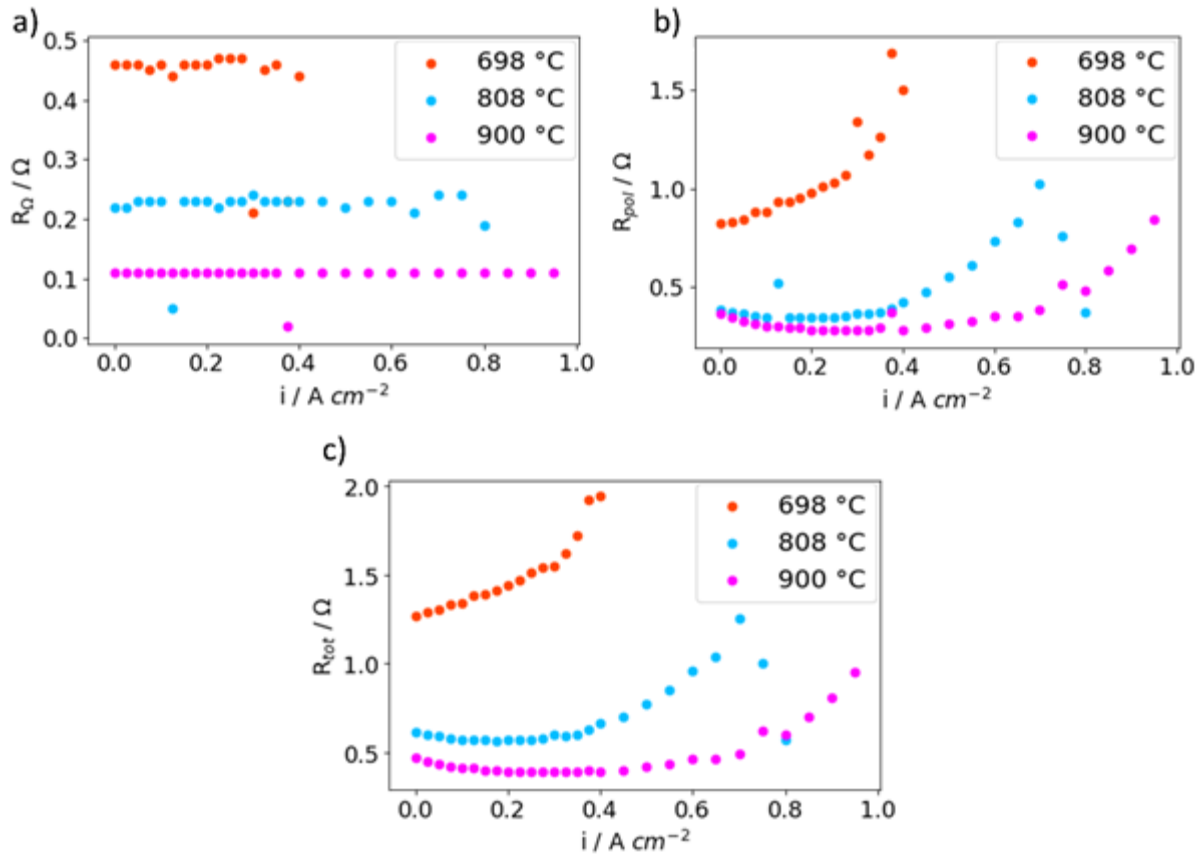


Figure 14: Comparison of the serial resistance ( $R_{\Omega}$ ), polarization resistance ( $R_{pol}$ ) and total resistance ( $R_{tot}$ ) dependent on the current density ( $i$ ) for three different temperatures. Measurement recorded in 80% CO<sub>2</sub> and 20% CO.

Figure 14 shows the relationship between the different resistances and the current density for the temperatures 698, 808 and 900 °C. The results displayed in Figure 14a confirm the previous observation, that the serial resistance  $R_{\Omega}$ , apart from few outliers, is current density independent. Since  $R_{\Omega}$  is the ohmic contribution of the metals and the materials of the cell, which are not involved in the electrolysis reaction, they only depend from the temperature. As

discussed in the previous section,  $R_{\Omega}$  decreases with increasing temperature, which is also confirmed in Figure 14a. The current dependence of the polarization resistance  $R_{pol}$  for different temperatures is displayed in Figure 14b. This dependence is similar to the temperature dependence for  $R_{\Omega}$ . However, the behavior of  $R_{pol}$  with increasing current density differs from  $R_{\Omega}$ . At 698 °C,  $R_{pol}$  increases linearly until approx.  $0.375 \text{ A cm}^{-2}$  and continues to increase with a steeper slope. For the temperatures 808 and 900 °C, the resistance slightly decreases until  $0.150 \text{ A cm}^{-2}$ . In the range of  $0.150$  and  $0.400 \text{ A cm}^{-2}$ ,  $R_{\Omega}$  shows a current independent behavior, which rises after  $0.400 \text{ A cm}^{-2}$ . Increasing resistance with raising current density is also consistent with the results obtained from the  $i/V$  measurements, since high current densities lead to higher  $\text{CO}_2$  consumptions, and thus to diffusion polarization, if the reactant delivery is not fast enough. However, at 808 °C,  $R_{pol}$  reaches a maximum at  $0.700 \text{ A cm}^{-2}$ , which is followed by a sharp drop. Figure 14c shows the total resistance  $R_{tot}$  of the cell. As it can be seen the course of the total resistance is similar to the course of the polarization resistance, indicating the serial resistance is negligible.

Since the polarization resistance  $R_{pol}$  is the sum of the resistances of the four RQ elements, the individual  $R_{RQ1-4}$  values were plotted against the current density, as it is shown in Figure 15.

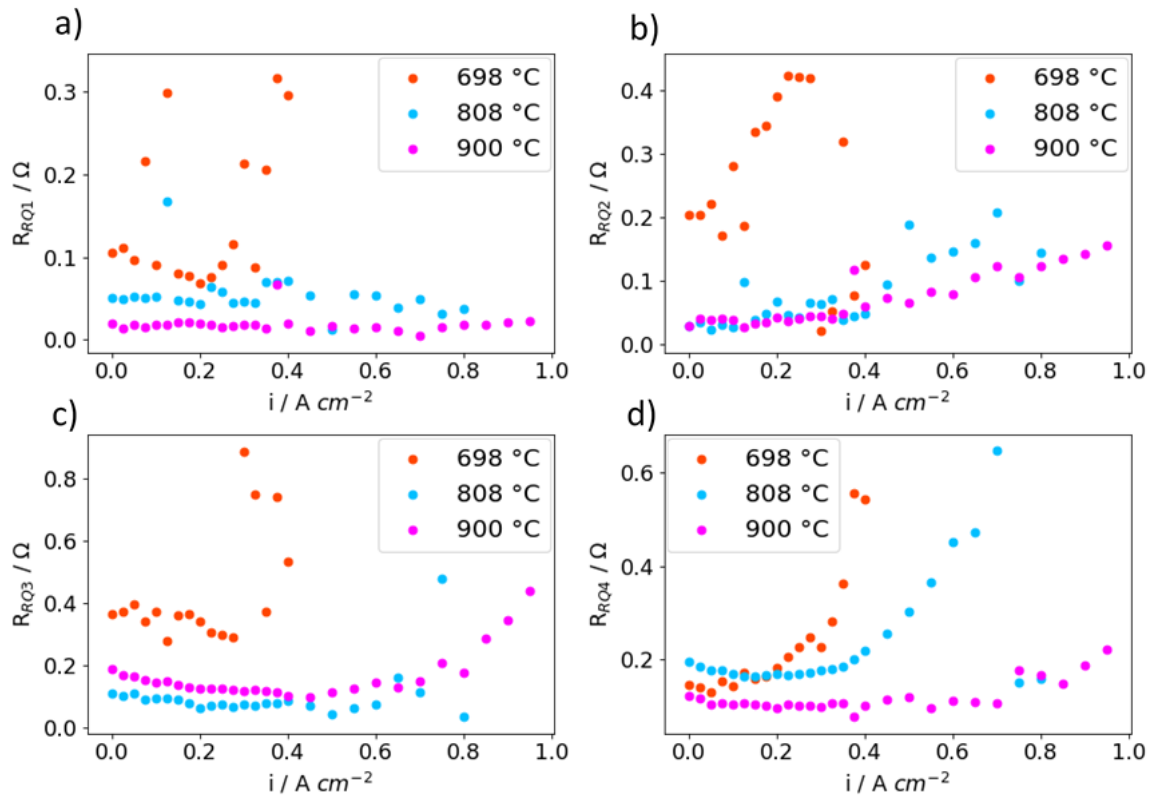


Figure 15: Comparison of the four polarization resistances ( $R_{RQ1-4}$ ) dependent on the current density ( $i$ ) for three different temperatures. Measurement recorded in 80%  $\text{CO}_2$  and 20%  $\text{CO}$ .

The aforementioned drop of  $R_{\text{pol}}$  after  $0.700 \text{ A cm}^{-2}$  at  $808 \text{ }^{\circ}\text{C}$  might be attributed to  $R_{\text{RQ3}}$  and  $R_{\text{RQ4}}$ , since their figures (Figure 15c – d) display a drop after approximately  $0.700 \text{ A cm}^{-2}$ . The results in Figure 15 reveal that the relationship between the resistances, current density and temperature is too complex and no clear tendency among these parameters can be seen.

The current dependence for different temperatures was further analyzed by a 2-dimensional representation of the DRT in dependence of the current density as shown in Figure 16.

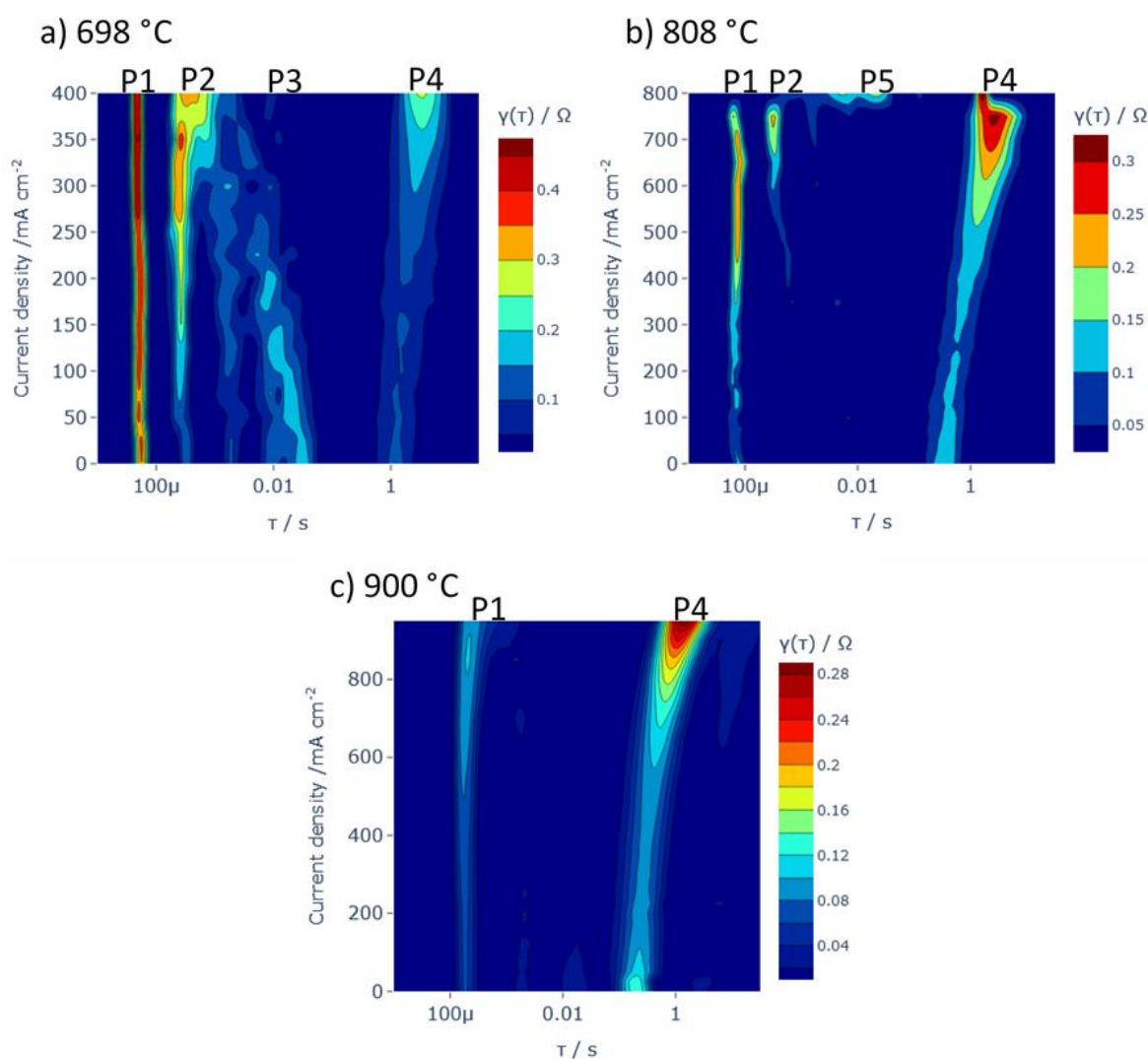


Figure 16: 2-D representation of the distribution of relaxation times (DRT) for different current densities, where  $\gamma(\tau)$  is the distribution function and  $\tau$  the relaxation time. Electrolysis was conducted in a mixture of 80%  $\text{CO}_2$  and 20%  $\text{CO}$  at 698, 808 and 900  $^{\circ}\text{C}$ .

The DRT was evaluated for the temperatures 698, 808 and 900  $^{\circ}\text{C}$ . Figure 16 reveals that with increasing temperature, the number of processes is decreasing. At 698  $^{\circ}\text{C}$ , four processes can

be observed, where the third one, P3, is assigned to a frequency range with two weak processes (22 Hz – 500 Hz). The most dominant process at low temperature is the first process P1, that appears at approximately 20 kHz. It can be seen that the intensity of P1 is not significantly affected by the current density, instead it is affected by the temperature, since  $\gamma(\tau)$  is decreasing with increasing temperature. The second process P2 occurs between 200  $\mu$ s and 785  $\mu$ s (5000 Hz – 1274 Hz). Similar to P1, P2 gets weaker with increasing temperature and completely disappears at 900 °C. At 698 °C and 808 °C the tendency of increasing  $\gamma(\tau)$  value with raising current density can be observed. Contrary to the first processes, P4 becomes stronger with increasing temperature and current density. This process occurs between 0.13 and 0.71 Hz. Another minor process, P5, can be found at 808 °C between 37 Hz and 333 Hz, which has no significant contribution to the total system.

In general, Figure 16 reveals similar to Figure 12, that the DRT results are not consistent with the previous determined model. The reasons for the inconsistency were explained in chapter 5.2.1.

### 5.2.3 50 % CO<sub>2</sub> and 50 % CO

As mentioned in the previous sections, due to the Boudouard equilibrium high CO amounts can lead to carbon deposition. Nonetheless, experiments with 50 % CO<sub>2</sub> and 50 % CO were conducted at 700, 808 and 900 °C. The corresponding EIS results are shown in Figure 17.

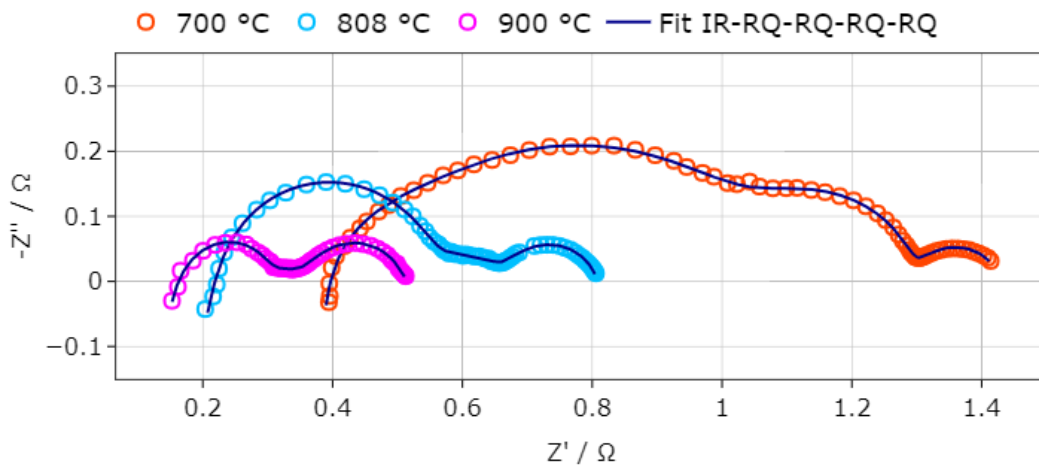


Figure 17: Nyquist plots of impedance spectra recorded during electrolysis in a mixture of 50% CO<sub>2</sub> and 50% CO for different temperatures at OCV.

Figure 17 reveals, that the shapes of the Nyquist plots varies with temperature. The plot for the EIS measurement at 700 °C displays three arcs. The width of the arcs decreases with increasing frequency. At 808 °C, only two arcs can be found, where the high frequency arc is the

dominating arc in terms of width and intensity. The two arcs are separated by a decreasing line, which might be the artifact of the second arc from the plot of 700 °C. The Nyquist plot for 900 °C shows also two arcs, however with similar width and heights. In general, Figure 17 reveals, that with increasing temperature the total resistance is decreasing, since the intercepts of the plots with the real axis are shifted to smaller values and the areas of the plots become smaller which is indicating a decreasing polarization resistance. This tendency is consistent with the temperature dependence for a gas mixture with 80 % CO<sub>2</sub> and 20 % CO, as described in previous sections.

Despite different shapes at different temperatures, the EIS data can be described using the equivalent circuit model as displayed in Figure 6. This model applies for measurements conducted at OCV, however with increasing current density different models must be developed.

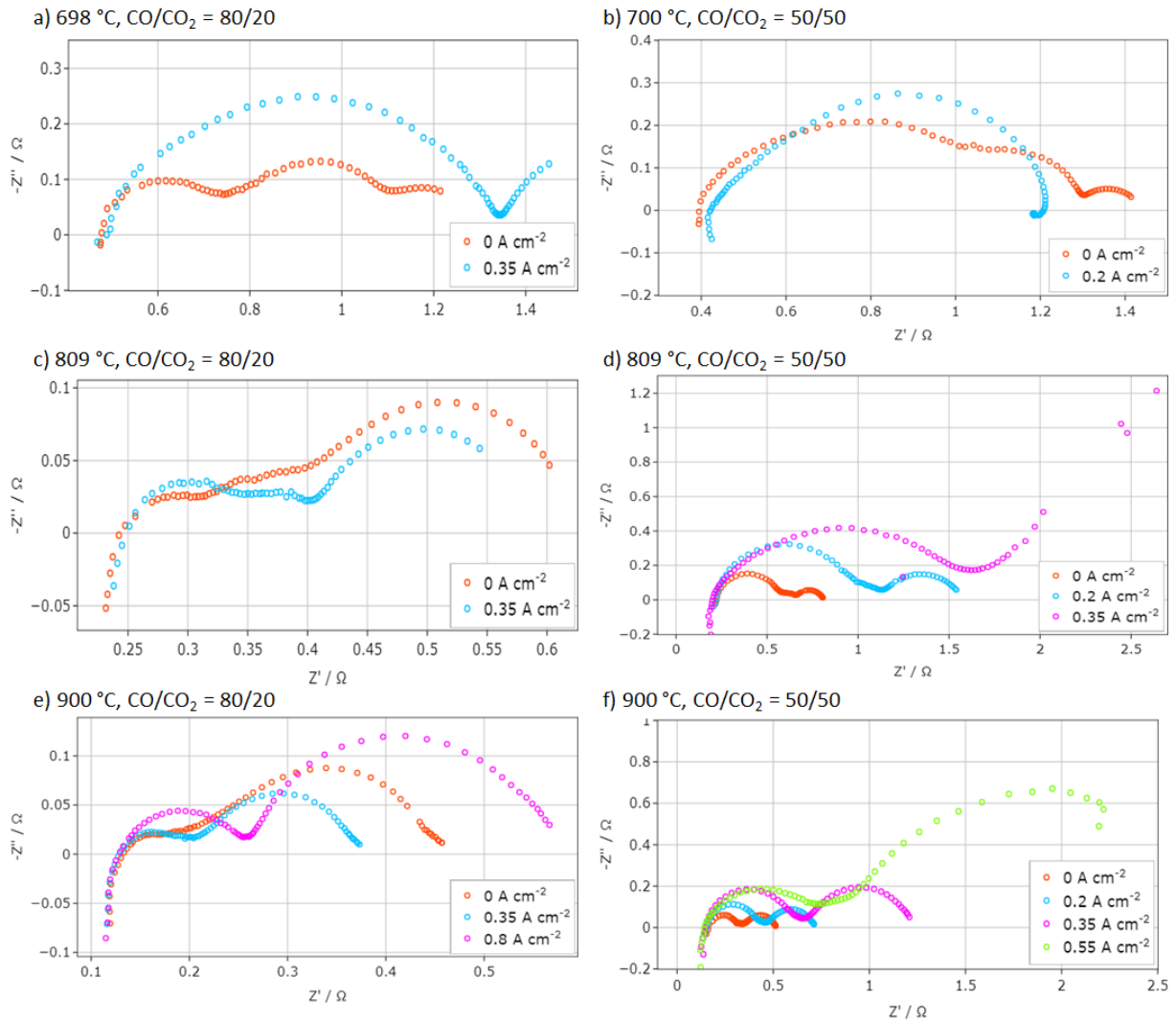


Figure 18: Nyquist plots of impedance spectra recorded during electrolysis in a mixture of CO<sub>2</sub>/CO (80/20 and 50/50) at different temperatures under various current densities.

Figure 18 reveals similarities and differences between the electrolysis in gas mixtures with  $\text{CO}_2/\text{CO}$  80/20 and 50/50. One similarity is the tendency of increasing polarization resistance with increasing current density. Another one is the number of arcs for each temperature, which however vary in their widths and heights depending on the gas mixture and the current density. A significant difference between electrolysis in these two gas mixtures are the total resistances, since reactions with 50/50  $\text{CO}_2/\text{CO}$  show higher resistances compared to electrolysis in a gas mixture with a lower CO content. This finding is consistent with the results gained from the  $i/V$  measurements. As explained in chapter 5.1, these observations might be due to the decreased  $\text{CO}_2$  content and the resulting diffusion polarization. Another reason might be attributed to coke formation which leads to a reduction of the active electrode area.

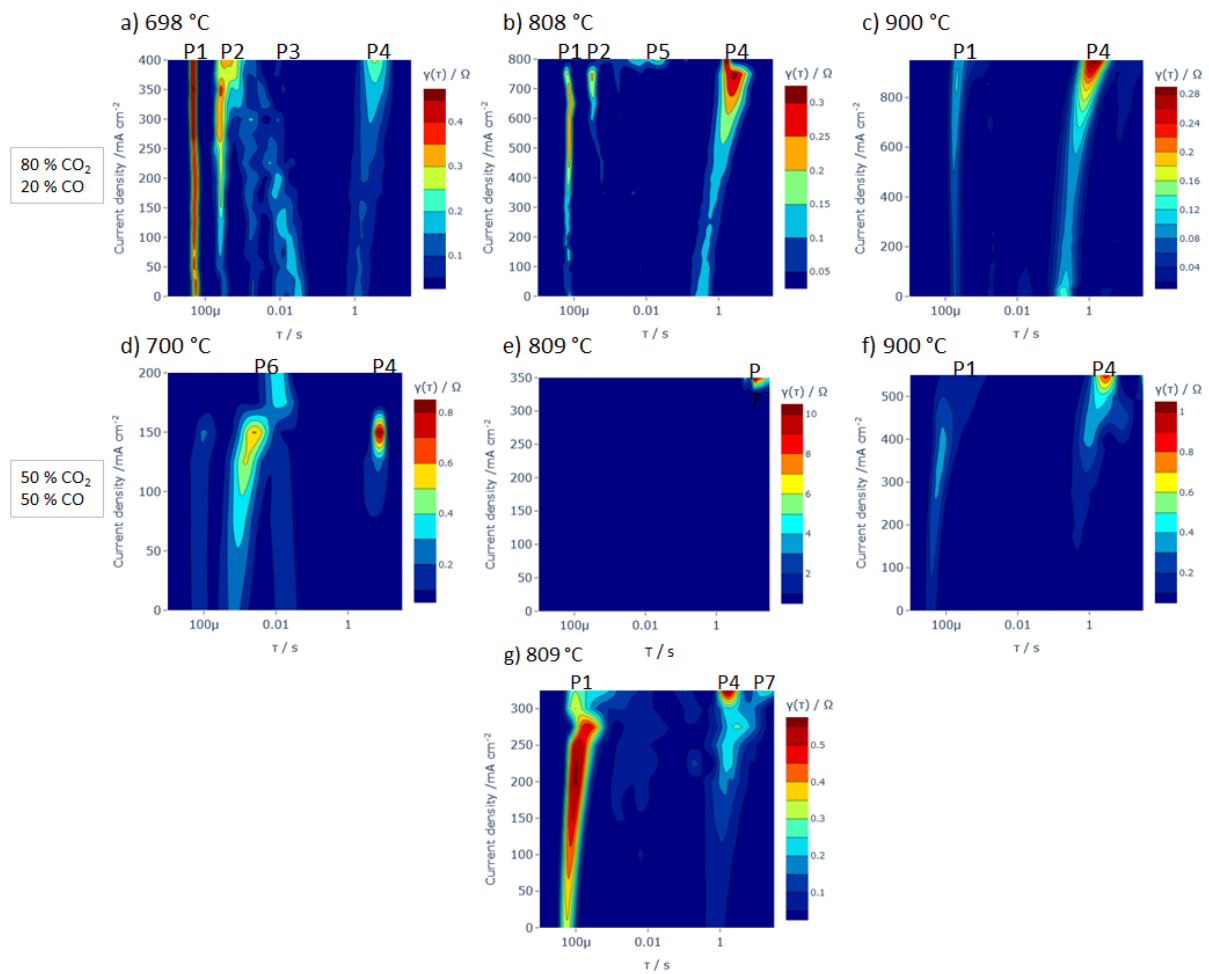


Figure 19: 2-D representation of the distribution of relaxation times (DRT) for different current densities, where  $\gamma(\tau)$  is the distribution function and  $\tau$  the relaxation time. a-c): DRT representation at three different temperature in a mixture with 80 %  $\text{CO}_2$  and 20 %  $\text{CO}$ . d-g): electrolysis in 50 %  $\text{CO}_2$  and 50 %  $\text{CO}$ . e) and g) belong to the same measurement, however in g) the maximum current density is  $325 \text{ mA cm}^{-2}$ .

Figure 19 displays a comparison of the DRT plots for the two mixtures 80/20 and 50/50 CO<sub>2</sub>/CO at the temperatures 700, 809 and 900 °C. As can be seen, in general systems with 50 % CO show higher  $\gamma(\tau)$  values, despite lower current densities applied to these systems compared to systems containing 20 % CO. Furthermore, it is apparent that the number and intensity of the processes vary with the gas mixture, as can be seen for the temperature 698/700 °C. P1 and P3 appear in Figure 19a, however they are missing in Figure 19d. This observation could be traced back to a different physicochemical behavior of the system with increasing CO amount. Another reason for the disappearance might be the predomination of certain processes, which lead to a scale with coarse intervals, overshadowing processes with lower intensities. This especially became apparent in Figure 19e, where P7 between 10 s – 25 s (0.04 Hz – 0.1 Hz) is the predominant process with a  $\gamma(\tau)$  value higher than 9  $\Omega$ . Not considering current densities higher than 325 mA cm<sup>-2</sup> shows a higher resolution in the high frequency domain as can be seen in Figure 19g. In comparison with the plot of 80 % CO<sub>2</sub> at 808 °C, the DRT plot for 50 % CO<sub>2</sub> at 809 °C (Figure 19g) displays the processes P1 and P4. Since P1 is broader for 50 % CO, it might be, that P2 merged with P1. The plots at 900 °C differ from each other in term of higher  $\gamma(\tau)$  values for 50 % CO, however in both systems the two processes P1 and P4 occur. At this point, a detailed explanation of the processes is not possible, since the amount of measurements and results are not sufficient.

## 6 Conclusion and Outlook

In summary, dry CO<sub>2</sub> electrolysis was investigated at temperatures between 700 and 900 °C at different current densities. Experiments with two different feed gas concentrations were conducted, first with 80 % CO<sub>2</sub> and 20 % CO, second with 50 % CO<sub>2</sub> and 50 % CO.

Within this work, two different electrochemical characterization methods, i/V and electrochemical impedance spectroscopy, were applied to investigate the impact of temperature, current density and gas feed composition on the performance of the high temperature electrolysis of CO<sub>2</sub> with CO.

The i/V curves reveal that the performance of the SOEC is highly temperature and gas composition dependent. Increasing temperature resulted in i/V curves with steeper slopes at higher current densities, which could be traced back to diffusion polarization due to a high CO<sub>2</sub> consumption and slower reactant delivery. Furthermore, a hysteresis at higher current densities was observed which became significant with increasing temperature and increasing CO amount. However, the CO<sub>2</sub>/CO ratio had a higher impact on the hysteresis formation than the temperature. This can be assigned most likely to the deterioration of the electrode due to sintering and coke formation. Further analysis reveals, that with increasing temperature the OCV and ASR values are decreasing, while the maximum current density at 1.4 V is increasing. The results show a higher performance for the system with a higher CO<sub>2</sub> amount. At 900 °C and 80 % CO<sub>2</sub>, a value of 1.52 A cm<sup>-2</sup> for the current density at 1.4 V could be achieved, whereas it was 0.66 A cm<sup>-2</sup> for 50 % CO<sub>2</sub> at the same temperature.

EIS measurements were used to gain insight into the different processes of the electrochemical systems. An equivalent circuit model for the EIS experiments with 80 % CO<sub>2</sub> could be determined, which consists of an inductor, a serial resistor and four RQ equivalent elements. This model is also applicable to systems with 50 % CO<sub>2</sub> and 50 % CO at low current densities. For a mixture containing 80 % CO<sub>2</sub> and 20 % CO, increasing temperature resulted in a shift of the intercepts with the real axis towards lower impedances, since the serial and the polarization resistances are decreasing. Raising temperature also led to a decrease of the number of the arcs. This observation is consistent with the 2-D representation of the DRT, which reveal less processes with increasing temperature. However, the determined equivalent circuit model and DRT are not consistent in terms of number of processes. This is probably due to difficult fitting



of weak processes which are occurring in the DRT. Furthermore, the determination of the DRT is strongly parameter dependent, which also might lead to the inconsistency. Another reason might be, that the determined model is providing a suitable fit, even though the occurring processes are not described sufficiently.

The equivalent circuit model was used to calculate the contributions of the individual RQ elements to determine the activation energies according to Arrhenius law. However, the results for the four processes could not be used for comparison with the literature, since no comparable systems were reported. The reported findings in the literature differed in terms of cell material, CO<sub>2</sub>/CO ratio, temperature and equivalent circuit model. This issue was partly circumvented by calculating the activation energy using the ASR value determined from the i/V curves, since in most reports the ASR value was used. The Arrhenius plot of the ASR for 80 % CO<sub>2</sub> reveals an almost linear course and an activation energy of 46.5 kJ mol<sup>-1</sup>. This value is 20 % smaller than the reported value of 58.2 kJ mol<sup>-1</sup> for a LSCM/GDC cathode in 70/30 CO<sub>2</sub>/CO.<sup>[26]</sup> However, the experimental determined value is in the same order of magnitude as the reported value.

Apart from the temperature dependence, the current dependence was investigated. The results reveal, that  $R_{\Omega}$  is temperature dependent but current independent, since  $R_{\Omega}$  is due to the ionic contribution of the electrolyte. Current dependency was found for  $R_{RQ}$ , since the resistance was increasing with increasing current density. This might be traced back to a higher CO<sub>2</sub> consumption at high current densities resulting in diffusion polarization.

EIS measurements conducted in a gas composition of 50 % CO<sub>2</sub> reveal similar electrochemical processes, current as well as temperature dependencies as for systems with 80 % CO<sub>2</sub>. The most significant difference between these two systems are the in general higher polarization resistances for a system with 50 % CO<sub>2</sub>. This work reveals that a high amount of CO has a negative impact on the performance of the cell.

Aiming at a high electrolysis performance, various parameters have to be optimized. The gas feed composition is the most crucial parameter, since it has the most significant impact on the performance, as was shown with the i/V curves and EIS measurements. Besides the composition, the temperature and the current densities have an impact on the performance and thus have to be adjusted. Another parameter, which was not considered in this work is the feed rate, which also could be used as a powerful tool to increase the electrolysis performance.

## 7 References

- [1] A. Tremel (Ed.) *SpringerBriefs in Applied Sciences and Technology*, Springer International Publishing; Imprint; Springer, Cham, **2018**.
- [2] G. Centi, E. A. Quadrelli, S. Perathoner, *Energy Environ. Sci.* **2013**, 6, 1711.
- [3] M. A. Laguna-Bercero, *Journal of Power Sources* **2012**, 203, 4.
- [4] H. G. Cha, K.-S. Choi, *Nature chemistry* **2015**, 7, 328.
- [5] R. Elder, D. Cumming, M. B. Mogensen in *Carbon dioxide utilisation. Closing the carbon cycle* (Eds.: P. Styring, E. A. Quadrelli, K. Armstrong), Elsevier, Amsterdam, Boston, Heidelberg, **2015**, pp. 183–209.
- [6] S. D. Ebbesen, R. Knibbe, M. Mogensen, *J. Electrochem. Soc.* **2012**, 159, F482-F489.
- [7] A. S. Veige, *Polyhedron* **2008**, 27, 3177.
- [8] Y. Alioshin, M. Kohn, A. Rothschild, J. Karni, *J. Electrochem. Soc.* **2016**, 163, F79-F87.
- [9] S. D. Ebbesen, M. Mogensen, *Journal of Power Sources* **2009**, 193, 349.
- [10] H. Zhang, J. Wang, S. Su, J. Chen, *International Journal of Hydrogen Energy* **2013**, 38, 9609.
- [11] M. Ni, *Chemical Engineering Journal* **2010**, 164, 246.
- [12] F. Bidrawn, G. Kim, G. Corre, J. T. S. Irvine, J. M. Vohs, R. J. Gorte, *Electrochem. Solid-State Lett.* **2008**, 11, B167.
- [13] Y. Shi, Y. Luo, N. Cai, J. Qian, S. Wang, W. Li, H. Wang, *Electrochimica Acta* **2013**, 88, 644.
- [14] "Impedance spectroscopy. Theory, experiment, and applications", can be found under <http://search.ebscohost.com/login.aspx?direct=true&scope=site&db=nlebk&db=nlabk&AN=128515>, **2005**.
- [15] V. F. Lvovich, *Impedance Spectroscopy*, John Wiley & Sons, Inc, Hoboken, NJ, USA, **2012**.
- [16] A. Lasia, *Electrochemical Impedance Spectroscopy and its Applications*, Springer New York, New York, NY, **2014**.
- [17] Jens Wallauer, "RelaxIS 3 Impedance Spectrum Analysis User's Manual".
- [18] N. Schlüter, S. Ernst, U. Schröder, *ChemElectroChem* **2019**, 6, 6027.
- [19] H. Schichlein, A. C. Müller, M. Voigts, A. Krügel, E. Ivers-Tiffée, *Journal of Applied Electrochemistry* **2002**, 32, 875.
- [20] J. Illig, T. Chrobak, M. Ender, J. P. Schmidt, D. Klotz, E. Ivers-Tiffée in *ECS Transactions*, ECS, **2010**, pp. 3–17.

- [21] C. Stoots, J. O'Brien, J. Hartvigsen, *International Journal of Hydrogen Energy* **2009**, *34*, 4208.
- [22] R. GREEN, C. LIU, S. ADLER, *Solid State Ionics* **2008**, *179*, 647.
- [23] S. H. Jensen, P. H. Larsen, M. Mogensen, *International Journal of Hydrogen Energy* **2007**, *32*, 3253.
- [24] NORECS, "ProboStat™. Sample holder cell system for electrical and other characterization at high temperatures and under controlled atmospheres".
- [25] L. Dittrich, M. Nohl, E. E. Jaekel, S. Foit, L.G.J. de Haart, R.-A. Eichel, *J. Electrochem. Soc.* **2019**, *166*, F971-F975.
- [26] X. Yue, J. T. S. Irvine, *Electrochem. Solid-State Lett.* **2012**, *15*, B31.
- [27] a) S. Xu, S. Li, W. Yao, D. Dong, K. Xie, *Journal of Power Sources* **2013**, *230*, 115; b) Y. Tian, H. Zheng, L. Zhang, B. Chi, J. Pu, J. Li, *J. Electrochem. Soc.* **2018**, *165*, F17-F23.

## 8 Appendix

Table 6: Total resistance ( $R_{tot}$ ) derived from EIS data, serial resistance ( $R_{\Omega}$ ), polarization resistance ( $R_{pol}$ ) dependent on the current density ( $i$ ) and temperature. Measurement recorded in 80% CO<sub>2</sub> and 20% CO.

	698 °C			808 °C			900 °C		
$i / A\ cm^{-2}$	$R_{tot} / \Omega$	$R_{\Omega} / \Omega$	$R_{pol} / \Omega$	$R_{tot} / \Omega$	$R_{\Omega} / \Omega$	$R_{pol} / \Omega$	$R_{tot} / \Omega$	$R_{\Omega} / \Omega$	$R_{pol} / \Omega$
0	1.27	0.46	0.82	0.61	0.22	0.38	0.47	0.11	0.36
0.025	1.29	0.46	0.83	0.6	0.22	0.37	0.45	0.11	0.34
0.005	1.3	0.46	0.84	0.59	0.23	0.36	0.43	0.11	0.32
0.075	1.33	0.45	0.88	0.58	0.23	0.35	0.42	0.11	0.31
0.100	1.34	0.46	0.88	0.57	0.23	0.34	0.41	0.11	0.3
0.125	1.38	0.44	0.93	0.57	0.05	0.52	0.41	0.11	0.3
0.150	1.39	0.46	0.93	0.57	0.23	0.34	0.4	0.11	0.29
0.175	1.41	0.46	0.95	0.56	0.23	0.34	0.4	0.11	0.29
0.200	1.44	0.46	0.98	0.57	0.23	0.34	0.39	0.11	0.28
0.225	1.47	0.47	1.01	0.57	0.22	0.34	0.39	0.11	0.28
0.250	1.51	0.47	1.03	0.57	0.23	0.34	0.39	0.11	0.28
0.275	1.54	0.47	1.07	0.58	0.23	0.35	0.39	0.11	0.28
0.300	1.55	0.21	1.34	0.60	0.24	0.36	0.39	0.11	0.28
0.325	1.62	0.45	1.17	0.59	0.23	0.36	0.39	0.11	0.28
0.350	1.72	0.46	1.26	0.60	0.23	0.37	0.39	0.11	0.29
0.375	1.92	0.23	1.69	0.63	0.23	0.39	0.4	0.02	0.37
0.400	1.94	0.44	1.5	0.66	0.23	0.42	0.39	0.11	0.28
0.450				0.70	0.23	0.47	0.4	0.11	0.29
0.500				0.77	0.22	0.55	0.42	0.11	0.31
0.550				0.85	0.23	0.61	0.43	0.11	0.32
0.600				0.96	0.23	0.73	0.46	0.11	0.35
0.650				1.04	0.21	0.83	0.46	0.11	0.35
0.700				1.25	0.24	1.02	0.49	0.11	0.38
0.750				1.00	0.24	0.76	0.62	0.11	0.51
0.800				0.57	0.19	0.37	0.6	0.11	0.48
0.850							0.7	0.11	0.58
0.900							0.81	0.11	0.69
0.950							0.95	0.11	0.84